

This copy is for your personal, non-commercial use only.

If you wish to distribute this article to others, you can order high-quality copies for your colleagues, clients, or customers by [clicking here](#).

Permission to republish or repurpose articles or portions of articles can be obtained by following the guidelines [here](#).

The following resources related to this article are available online at www.sciencemag.org (this information is current as of November 15, 2010):

Updated information and services, including high-resolution figures, can be found in the online version of this article at:

<http://www.sciencemag.org/cgi/content/full/329/5990/444>

Supporting Online Material can be found at:

<http://www.sciencemag.org/cgi/content/full/329/5990/444/DC1>

This article **cites 27 articles**, 4 of which can be accessed for free:

<http://www.sciencemag.org/cgi/content/full/329/5990/444#otherarticles>

This article has been **cited by** 1 articles hosted by HighWire Press; see:

<http://www.sciencemag.org/cgi/content/full/329/5990/444#otherarticles>

This article appears in the following **subject collections**:

Neuroscience

<http://www.sciencemag.org/cgi/collection/neuroscience>

Dnmt3a-Dependent Nonpromoter DNA Methylation Facilitates Transcription of Neurogenic Genes

Hao Wu,^{1*} Volkan Coskun,² Jifang Tao,² Wei Xie,³ Weihong Ge,¹ Kazuaki Yoshikawa,⁴ En Li,⁵ Yi Zhang,⁶ Yi Eve Sun^{1,2*}

DNA methylation at proximal promoters facilitates lineage restriction by silencing cell type-specific genes. However, euchromatic DNA methylation frequently occurs in regions outside promoters. The functions of such nonproximal promoter DNA methylation are unclear. Here we show that the *de novo* DNA methyltransferase Dnmt3a is expressed in postnatal neural stem cells (NSCs) and is required for neurogenesis. Genome-wide analysis of postnatal NSCs indicates that Dnmt3a occupies and methylates intergenic regions and gene bodies flanking proximal promoters of a large cohort of transcriptionally permissive genes, many of which encode regulators of neurogenesis. Surprisingly, Dnmt3a-dependent nonproximal promoter methylation promotes expression of these neurogenic genes by functionally antagonizing Polycomb repression. Thus, nonpromoter DNA methylation by Dnmt3a may be used for maintaining active chromatin states of genes critical for development.

De novo DNA methyltransferases Dnmt3a and Dnmt3b and maintenance methyltransferase Dnmt1 covalently modify mammalian genomes by cytosine methylation, an epigenetic mark that is essential for normal development and primarily occurs at CpG dinucleotides (1). Most CpG-rich regions (CpG islands) overlap with proximal promoters, where DNA methylation is linked to gene silencing (2). However, unbiased genome-wide analyses have shown that DNA methylation is widespread across the euchromatic portion of mammalian genomes and predominantly takes place in regions outside proximal promoters, including intergenic regions and gene bodies (2, 3), where tissue-specific DNA methylation is frequently localized (4). Deletion of Dnmt1 or treatment with Dnmt inhibitors in dividing somatic cells can lead to global DNA hypomethylation, chromosomal instability, and compromised cell-cycle progression, thereby hindering functional analysis of DNA methylation in self-renewing tissue-specific stem cells. Unlike Dnmt1 or Dnmt3b (the deletion of which, in mice, leads to early embryonic lethality), Dnmt3a is not required for maintaining methylation at heterochromatic repeat regions, and *Dnmt3a*-null mice appear to be grossly normal at birth (5, 6). However, mice lacking *Dnmt3a* do acquire develop-

mental defects postnatally and die prematurely (5), suggesting a specific role for Dnmt3a in regulating euchromatic methylation and postnatal development.

The function of DNA methylation in the postnatal brain is of particular interest, because brain-specific deletion of DNA methylation-related machineries results in postnatal neurodevelopmental abnormalities and premature death in mice (7, 8). Multiple isoforms of Dnmt3a/3b are expressed in mouse embryonic stem (ES) cells, but only the Dnmt3a full-length variant is expressed in diverse regions of the postnatal brain (7, 9), including subependymal/subventricular zones (SEZ/SVZ) of the forebrain and the hippocampal dentate gyrus (fig. S1), two neurogenic regions in which neural stem cells (NSCs) persist throughout life (10). In *Dnmt3a*-null mice, quantification of doublecortin (Dcx)-positive immature neurons demonstrated that postnatal neurogenesis at both neurogenic zones was impaired (Fig. 1, A and B, and fig. S2) (11). However, the decrease in the number of newborn neurons was unlikely to be caused by changes in proliferation and/or survival of postnatal NSCs (fig. S3, A and B). To further evaluate the function of Dnmt3a in NSCs, we derived monolayer NSC cultures from wild-type (WT) and *Dnmt3a*-null [knockout (KO)] mice. Though Dnmt3a was dispensable for maintaining NSCs in an undifferentiated and proliferating state (fig. S3, C to F), upon mitogen withdrawal, differentiating *Dnmt3a*-null cells produced more than 10-fold fewer Tuj1+/Map2+ neurons (Fig. 1, C and D) and more glial cells, as compared with WT cells (fig. S4). To exclude the possibility that impaired neurogenic potential of *Dnmt3a*-null NSCs resulted from secondary effects after long-term *Dnmt3a*-deletion, postnatal NSCs were isolated from mice homozygous for floxed alleles of Dnmt3a (*Dnmt3a*^{fllox/fllox}) (12) and were infected with control or Cre-expressing lentiviruses (fig. S5, A and B). Differentiation analyses indicated that acute *Dnmt3a*-deletion (5-day) also impaired

neuronal differentiation (fig. S5C). Moreover, the neurogenesis deficit in *Dnmt3a*-null cultures was rescued by re-expressing physiological levels of WT Dnmt3a, but not catalytically inactive mutant Dnmt3a (Fig. 1D and fig. S6, A and B) (13). Expression of other Dnmt proteins and global DNA methylation patterns remained largely unchanged in *Dnmt3a*-null and rescued NSCs (fig. S6, B to D). Thus, specific and cell-autonomous functions of Dnmt3a are required for neurogenesis from postnatal NSCs.

To investigate the mechanism underlying Dnmt3a-dependent neurogenesis, we mapped genome-wide Dnmt3a occupancy in postnatal NSCs by chromatin immunoprecipitation (ChIP) (N⁷ Ab in fig. S1B) combined with whole-genome tiling microarrays (ChIP-chip). We identified 30,417 Dnmt3a binding-sites with high-confidence (false discovery rate < 1%). Quantitative polymerase chain reaction (qPCR) analysis confirmed that all 20 randomly selected loci showed significant enrichment for Dnmt3a (fig. S7A). Control ChIP-chip experiments in *Dnmt3a*-null NSCs did not yield specific enrichment (fig. S8A), confirming the specificity of Dnmt3a ChIP results. Most Dnmt3a binding sites were located in gene-rich euchromatic regions, as 80.7% of all binding sites were within gene bodies or 50-kb intergenic regions up- and downstream of annotated genes (fig. S9A). Mapping Dnmt3a binding sites to regions flanking transcription start sites (TSSs) revealed two categories of Dnmt3a targets (Fig. 2A). The first group (*n* = 2449 targets) was characterized by the presence of CpG islands, which generally harbor high levels of trimethylation of lysine 4 on histone H3 (H3K4me3), a histone mark indicative of transcriptionally permissive chromatin states, within their proximal promoter regions (hereafter referred to as CpG-rich/H3K4me3-high targets) (Fig. 2A and fig. S8, A to C). On these targets, Dnmt3a was generally excluded from H3K4me3-high, CpG-rich proximal promoters, but was enriched in inter- and intragenic regions flanking CpG islands (black in Fig. 2B), possibly because of the inhibitory effect of H3K4 methylation on Dnmt3a binding to chromatin (14). The other group of Dnmt3a targets (*n* = 1096) was associated with CpG-poor promoters and low levels of H3K4me3 (Fig. 2A and fig. S8, A to C). Dnmt3a binding sites on these H3K4me3-low targets frequently overlapped with proximal promoters (orange in Fig. 2B). Subsequent genome-wide methylated DNA immunoprecipitation assays (MeDIP-chip) revealed that Dnmt3a-dependent DNA methylation was restricted to Dnmt3a binding sites (Fig. 2C and fig. S9B). Locus-specific methylation assays (MeDIP-qPCR, bisulphite sequencing, or mass spectrometry) further demonstrated that, on H3K4me3-high targets (for instance, *Dlx2*, *Gbx2*), Dnmt3a-dependent DNA methylation was present in regions encompassing proximal promoters, but not within core promoter regions (Fig. 2, C and D, and figs. S7; S10, A and B; and S11, B and C). In contrast, Dnmt3a-mediated methylation was enriched at proximal promoters of H3K4me3-low

¹Department of Molecular and Medical Pharmacology, University of California Los Angeles (UCLA), Los Angeles, CA 90095, USA. ²Department of Psychiatry and Biobehavioral Sciences, Intellectual Development and Disabilities Research Center at Semel Institute for Neuroscience, UCLA, Los Angeles, CA 90095, USA. ³Molecular Biology Institute, UCLA School of Medicine, Los Angeles, CA 90095, USA. ⁴Laboratory of Regulation of Neuronal Development, Institute for Protein Research, Osaka University, Suita, Osaka, 565-0871, Japan. ⁵Novartis Institutes for Biomedical Research, Cambridge, MA 02139, USA. ⁶Howard Hughes Medical Institute, Department of Biochemistry and Biophysics, Lineberger Comprehensive Cancer Center, University of North Carolina at Chapel Hill, Chapel Hill, NC 27599, USA.

*To whom correspondence should be addressed. E-mail: ysun@mednet.ucla.edu (Y.E.S.); haowu7@gmail.com (H.W.)

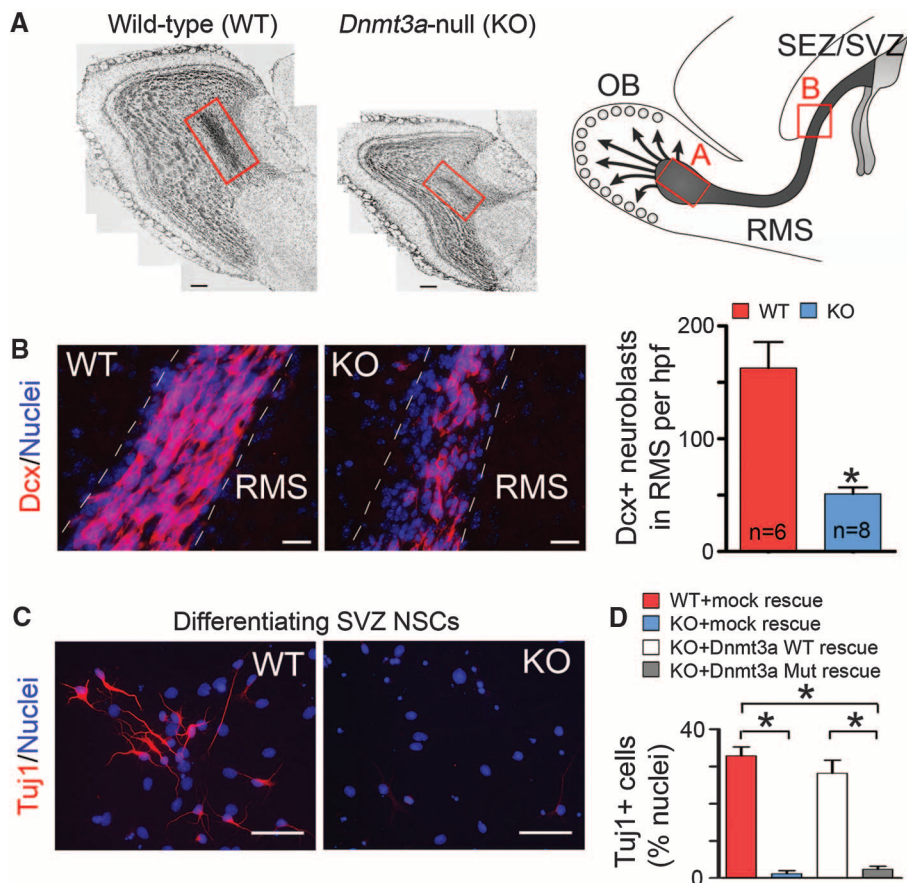


Fig. 1. Essential roles of Dnmt3a in postnatal neurogenesis. **(A)** Cell nuclei staining of olfactory bulb (OB) in WT and KO mice at postnatal day (P) 24. The schematic on the right outlines the postnatal neurogenesis from SEZ/SVZ NSCs, and the red boxes denote the portion of the rostral migratory stream (RMS) with newborn neurons entering the OB. Note that both the OB size and the number of newborn neurons in KO mice (red box) are reduced. Arrows indicate radially migrating immature neurons in the postnatal OB. Scale bars, 200 μ m. **(B)** Immunohistochemistry and quantification of Dcx+ neuroblasts in WT and KO RMS (P21 to P24). Hpf, high-power field; *n*, number of fields from three pairs of littermate mice. Error bars indicate SEM (**P* < 0.01). Scale bars, 50 μ m. **(C)** Immunocytochemistry of the immature neuronal marker Tuj1 in differentiating WT and KO SEZ/SVZ cultures. Scale bars, 50 μ m. **(D)** Quantification of Tuj1+ neurons in differentiating WT, KO, and rescued NSC cultures. Error bars indicate SEM (**P* < 0.01, *n* = 10 to 15).

targets (e.g., *Gfap*) (Fig. 2, C and D, and fig. S7C). Although DNA methylation changes have been reported after long-term cell culture (15), short-term in vitro culturing in our experiments did not significantly alter promoter DNA methylation levels, either globally or on Dnmt3a targets (fig. S10, B and C). Collectively, these data indicate that Dnmt3a may occupy and methylate defined genomic regions associated with both transcriptionally active and inactive genes in postnatal NSCs.

To gain insights into the biological function of Dnmt3a targets, we performed gene ontology analysis with Dnmt3a targets. Genes functionally related to nervous system development (*P* = 1.5×10^{-30} , hypergeometric test) and neurogenesis (*P* = 6.5×10^{-19}) were significantly enriched within H3K4me3-high Dnmt3a targets, whereas genes involved in development of non-neuronal lineage were enriched in H3K4me3-low Dnmt3a targets (fig. S8D). H3K4me3-high targets were transcribed at medium-to-high levels in postnatal NSCs, signif-

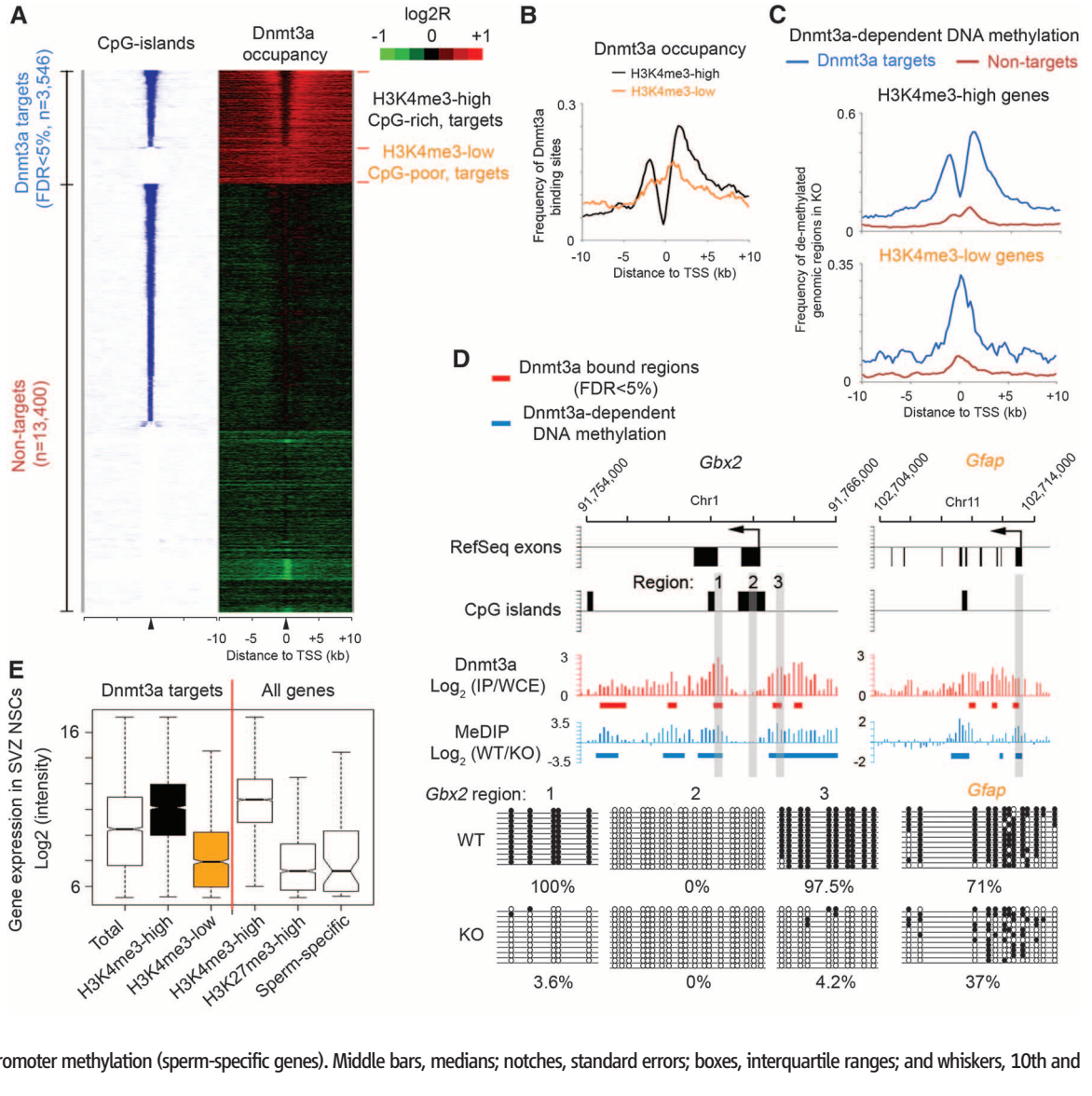
icantly higher than expression levels of H3K4me3-low targets, or genes marked by an inactive histone modification H3K27me3 or a group of sperm-specific genes with proximal promoter DNA methylation (Fig. 2E).

To establish a direct link between Dnmt3a binding and transcriptional regulation, we performed gene-expression profiling and identified a total of 2275 genes (1253 up-regulated and 1022 down-regulated in *Dnmt3a*-null mice) that are differentially expressed between undifferentiated WT and KO NSCs. Dnmt3a binding sites were detected within 10-kb up- and downstream of the TSSs of 942 differentially expressed transcripts (41.4% of 2275 genes, *P* = 1.36×10^{-122} , Fisher's exact test) (Fig. 3A), indicating that a significant fraction of Dnmt3a-dependent expression changes represent a direct effect of Dnmt3a binding. Although DNA methylation has been primarily associated with repression, Dnmt3a targets were significantly enriched in both up- and down-

regulated genes in KO NSCs (536 up-regulated, *P* = 3.3×10^{-71} ; 406 down-regulated, *P* = 1.9×10^{-43}). Notably, genes with known roles in postnatal neurogenesis (for example, *Dlx2*, *Sp8*, and *Neurog2*) were among the down-regulated Dnmt3a targets in KO NSCs (fig. S11A) (16, 17). In contrast, several Dnmt3a targets involved in astroglial and oligodendroglial differentiation (e.g., *Sparc11*, *Nkx2-2*) were up-regulated in KO cultures. Gene-expression analyses with differentiating NSCs also supported the conclusion that Dnmt3a promotes transcription of neurogenic targets while repressing glial differentiation genes (table S1 and supporting online material text). Further in vivo analysis revealed fewer Dlx2+ and Sp8+ progenitors/neuroblasts and their subtype-specific interneuron progenies in KO mice (fig. S12, A to E), and re-expression of *Dlx2* in KO cells substantially rescued the neurogenesis defect (fig. S12F). Taken together, these results indicate that Dnmt3a is not only involved in transcriptional repression but also required by postnatal NSCs to promote expression of many direct targets, including key neurogenic factors, thereby contributing to postnatal neurogenesis.

The percentage of H3K4me3-high promoters in down-regulated targets (65.4% of 406 genes) was significantly higher than that expected by chance (*P* = 7.7×10^{-8}), and DNA demethylation was predominantly detected outside proximal promoters of these down-regulated targets in KO NSCs (Fig. 3A and fig. S11, B and C). In contrast, DNA demethylation may repress transcription by antagonizing active histone marks (Fig. 3A) (15, 18, 19), growing evidence suggests that non-promoter DNA methylation positively correlates with transcription of tissue-specific genes or genes on the active X chromosome (2, 20). DNA methylation also inversely correlates with the presence of H3K27me3 in human cancer cell lines or on the transcriptional regulatory region for the imprinting locus *Rasgrf1* (21, 22). Therefore, we hypothesized that Dnmt3a-dependent nonpromoter DNA methylation may facilitate transcription by antagonizing H3K27me3. To test this idea, we examined genome-wide H3K27me3 occupancy in WT and KO NSCs. Our analysis revealed that *Dnmt3a*-deficiency resulted in an increase in H3K27me3 levels across large genomic regions associated with many down-regulated targets (green in Fig. 3B and fig. S11, B and C), whereas the increase in H3K27me3 levels in KO NSCs was observed less often on up-regulated targets (red in Fig. 3B; *P* = 1.8×10^{-20}) or targets without changes in expression (blue in Fig. 3B; *P* = 1.6×10^{-28}). Acute ablation of Dnmt3a also led to a significant increase in H3K27me3 levels on down-regulated targets, suggesting that the antagonism between Dnmt3a and H3K27me3 is unlikely due to

Fig. 2. Dnmt3a occupies and methylates defined regions at both transcriptionally active and inactive genes. **(A)** Heat map representations of CpG islands (blue/white) and Dnmt3a (red/green) are shown for both Dnmt3a targets and nontargets. Red/blue represents enrichment, whereas green/white represents no enrichment. Genes were rank-ordered by CpG-island length within 4-kb regions flanking TSSs. FDR, false discovery rate; *n*, number of genes. **(B)** Distribution of Dnmt3a binding-sites within regions flanking TSSs of H3K4me3-high/CpG-rich and H3K4me3-low/CpG-poor targets. **(C)** Distribution of Dnmt3a-dependent DNA methylation within regions flanking TSSs of CpG-rich and CpG-poor genes. **(D)** Dnmt3a occupancy and Dnmt3a-dependent DNA methylation within representative CpG-rich/H3K4me3-high (*Gbx2*) and CpG-poor/H3K4me3-low (*Gfap*) targets. Regions validated by bisulphite sequencing are shown in gray. IP, immunoprecipitation; WCE, whole-cell extract. **(E)** Box plots of expression levels in WT postnatal NSCs are shown for genes associated with Dnmt3a, H3K4me3, H3K27me3, and proximal promoter methylation (sperm-specific genes). Middle bars, medians; notches, standard errors; boxes, interquartile ranges; and whiskers, 10th and 90th percentiles.



nonspecific compensation after long-term *Dnmt3a* deletion (fig. S5D). Thus, Dnmt3a-dependent non-promoter DNA methylation may facilitate the expression of many H3K4me3-high targets by reducing H3K27me3 levels.

Because *Dnmt3a* deficiency did not change the overall levels of H3K27me3 or Polycomb repression complex 2 (PRC2) that catalyzes trimethylation of H3K27 (fig. S13, A and B), we considered a model in which Dnmt3a functioned to antagonize PRC2 binding to chromatin. ChIP-chip analysis of Suz12 and Ezh2, two core subunits of PRC2, revealed that *Dnmt3a* deficiency led to a significant increase in Suz12 occupancy on Dnmt3a targets with a marked increase in H3K27me3 in KO NSCs ($P < 2.2 \times 10^{-16}$); similar results were obtained for Ezh2 (Fig. 4A and fig. S11, D and E). The increase of PRC2/H3K27me3 levels on these Dnmt3a targets was specific, as other PRC2 targets that were not targeted by Dnmt3a (e.g., *Hoxb9* in Fig. 4A) were associated with similar levels of PRC2/H3K27me3 in WT and KO NSCs. To

evaluate whether Dnmt3a enzymatic activity is required for opposing PRC2 binding, we analyzed *Dnmt3a*-null NSCs rescued with physiological levels of WT or catalytically inactive mutant Dnmt3a. In rescued KO NSCs, both WT and mutant Dnmt3a re-occupied Dnmt3a targets (fig. S14A), but only WT Dnmt3a restored DNA methylation levels (fig. S14, B and C). WT, but not mutant Dnmt3a, reversed aberrantly elevated levels of PRC2/H3K27me3 on down-regulated Dnmt3a targets in KO NSCs (Fig. 4B), indicating that Dnmt3a-dependent DNA methylation, but not Dnmt3a binding, is incompatible with PRC2 occupancy and may directly antagonize the PRC2 binding. Therefore, we tested recruitment of PRC2 complexes to in vitro DNA-methylated chromatin arrays consisting of recombinant *Xenopus* octamers (23, 24), which are free of any other epigenetic marks existing on endogenous chromatin that may also regulate PRC2 recruitment (fig. S15). This analysis indicated that DNA methylation alone partially inhibited PRC2 binding to

chromatin arrays (Fig. 4C). Furthermore, PRC2 deficiency in *Dnmt3a*-null NSCs could substantially restore the expression of neurogenic targets and rescue neuronal differentiation defects (Fig. 4D and fig. S13, C and D). Dnmt3a-dependent DNA methylation may, therefore, down-regulate H3K27me3 levels on transcriptionally active targets by antagonizing binding of PRC2 to chromatin.

Together, these results suggest that the DNA methyltransferase Dnmt3a not only mediates repression in self-renewing postnatal NSCs by methylating proximal promoters, but also promotes transcription of targets, including neurogenic genes, by antagonizing Polycomb repression through nonproximal promoter methylation (fig. S16). The positive correlation between nonpromoter DNA methylation and transcription on Dnmt3a targets is also observed during mouse ES cell differentiation into neural progenitors, as well as in vivo analysis of multiple adult tissues, suggesting that this finding may be generally applicable to other

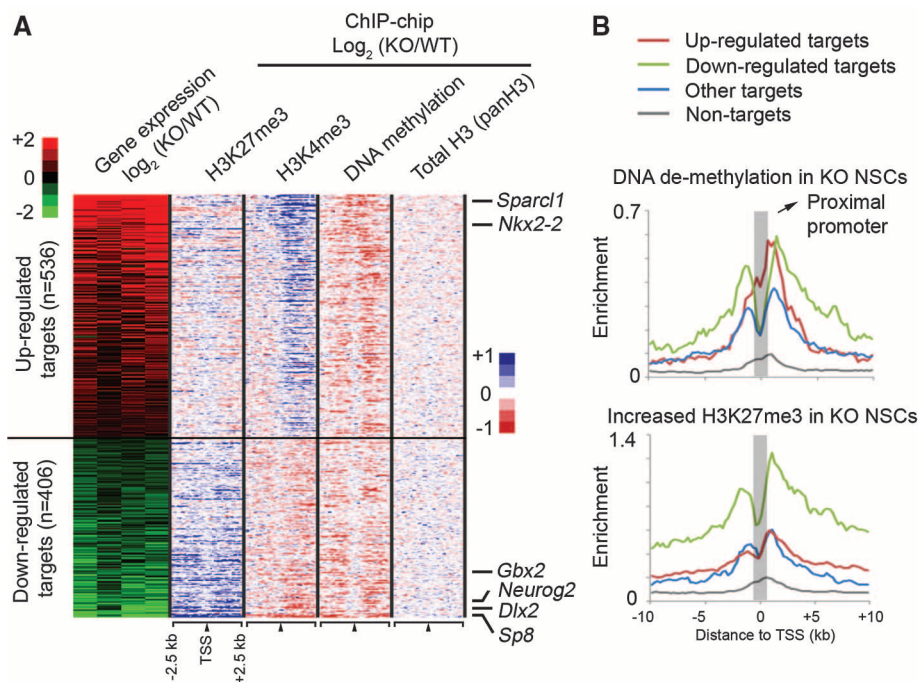
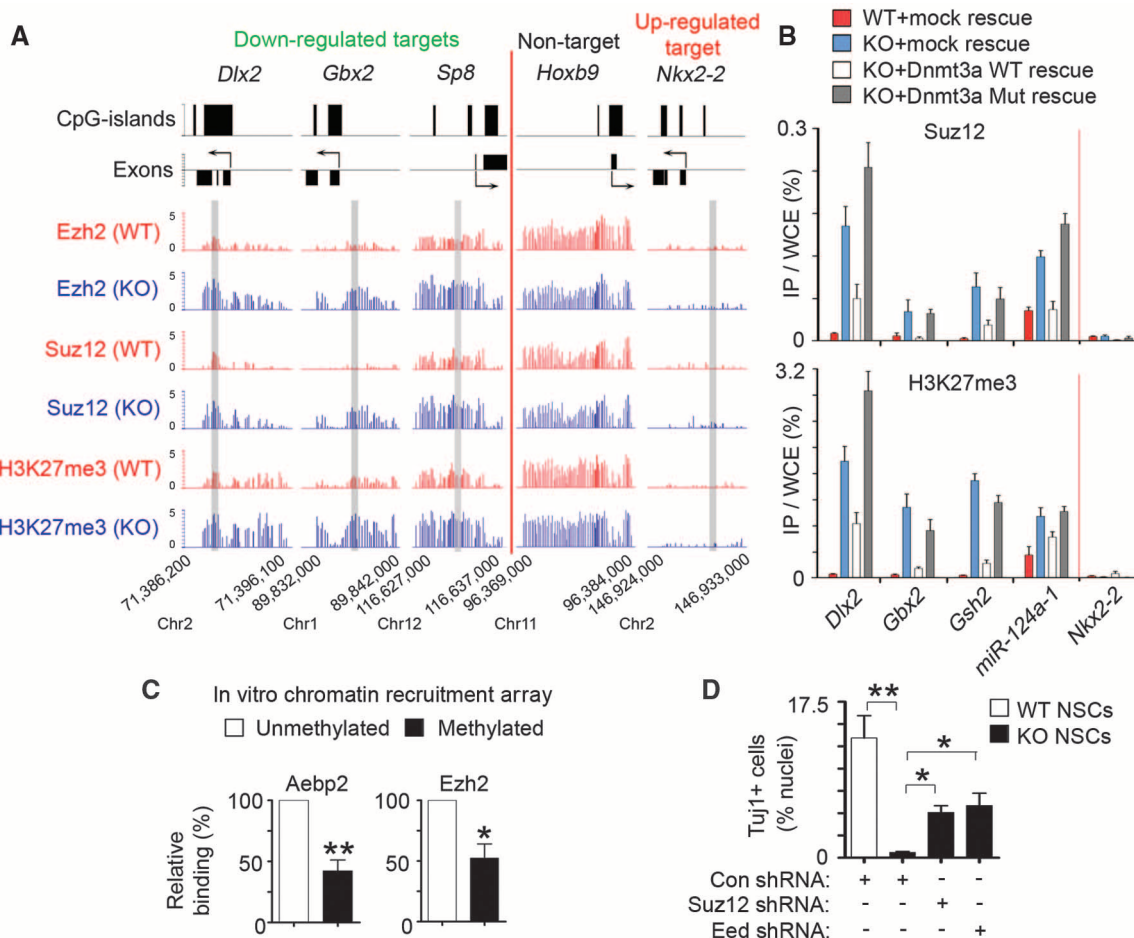


Fig. 3. Dnmt3a promotes transcription through nonpromoter methylation. **(A)** Heat map representations of relative changes in expression (from four experiments), DNA methylation, H3K4me3, H3K27me3, and total histone H3 levels (panH3) between KO and WT NSCs are shown for differentially expressed Dnmt3a targets, which are ranked by changes in expression between KO and WT NSCs. *n*, number of targets. **(B)** Distributions of DNA demethylation and H3K27me3 increase in KO NSCs are shown for up-regulated targets (red), down-regulated targets (green), targets without expression changes (blue), and nontargets (gray).

Fig. 4. Dnmt3a promotes transcription by antagonizing Polycomb repression. **(A)** Ezh2, Suz12, and H3K27me3 occupancy at representative genes in WT and KO NSCs. Regions analyzed by ChIP-qPCR (in fig. S11E) are shaded in gray. **(B)** Quantitative PCR analysis of Suz12 and H3K27me3 at representative targets in WT, KO, and rescued NSCs. **(C)** Relative binding of PRC2 subunits on methylated or unmethylated chromatin arrays was quantified by densitometry (**P* = 0.027, *n* = 4 experiments; ***P* = 0.0013, *n* = 6). **(D)** Quantification of Tuj1+ neurons in control and PRC2-deficient differentiating NSCs. Error bars indicate SEM of randomly selected fields from two independent cultures (**P* < 0.05; ***P* < 0.01).



developmental processes (figs. S17 and S18). Embryonic neurogenesis is largely intact in *Dnmt3a*-null mice (10), perhaps because embryonic neuroblasts are primarily generated from neuroepithelial progenitors where Dnmt3b is still highly expressed (13). Furthermore, Polycomb repression can also be inhibited by H3K27me3 demethylase (e.g., Jmjd3), which may be recruited by H3K4 methyltransferases Mll to promoters of neurogenic factors during embryonic and/or postnatal neurogenesis (16, 25). Non-proximal promoter DNA methylation established by Dnmt3a may, therefore, represent an additional layer of epigenetic regulation of Polycomb repression in somatic cells. Although PRC2 may directly interact with Dnmt proteins (26, 27), it seems that DNA methyltransferases (for instance, catalytically inactive Dnmt3a) may coexist with high levels of PRC2 occupancy at the same genomic loci (27), only in the absence of de novo DNA methylation. Thus, Polycomb proteins may contribute to the initial recruitment of Dnmt, the accumulation of which leads to local de novo DNA methylation, thereby dampening Polycomb repression. Given that both DNA methylation and Polycomb pathways are indispensable for normal development and are implicated in diseases, including neurological disorders and cancer (21, 28), it will be of interest to fully elucidate mechanisms by which these two epigenetic machineries are targeted to specific genomic loci and are cross-regulated.

References and Notes

- R. Jaenisch, A. Bird, *Nat. Genet.* **33**, 245 (2003).
- M. M. Suzuki, A. Bird, *Nat. Rev. Genet.* **9**, 465 (2008).
- R. Lister *et al.*, *Nature* **462**, 315 (2009).
- R. A. Irizarry *et al.*, *Nat. Genet.* **41**, 178 (2009).
- M. Okano, D. W. Bell, D. A. Haber, E. Li, *Cell* **99**, 247 (1999).
- E. Li, T. H. Bestor, R. Jaenisch, *Cell* **69**, 915 (1992).
- S. Nguyen, K. Meletis, D. Fu, S. Jhaveri, R. Jaenisch, *Dev. Dyn.* **236**, 1663 (2007).
- M. Chahrour, H. Y. Zoghbi, *Neuron* **56**, 422 (2007).
- J. Feng, H. Chang, E. Li, G. Fan, *J. Neurosci. Res.* **79**, 734 (2005).
- H. Suh, W. Deng, F. H. Gage, *Annu. Rev. Cell Dev. Biol.* **25**, 253 (2009).
- Materials and methods are available as supporting material on Science Online.
- M. Kaneda *et al.*, *Nature* **429**, 900 (2004).
- T. Chen, N. Tsujimoto, E. Li, *Mol. Cell. Biol.* **24**, 9048 (2004).
- J. Otani *et al.*, *EMBO Rep.* **10**, 1235 (2009).
- A. Meissner *et al.*, *Nature* **454**, 766 (2008).
- D. A. Lim *et al.*, *Nature* **458**, 529 (2009).
- R. R. Waclaw *et al.*, *Neuron* **49**, 503 (2006).
- S. K. Ooi *et al.*, *Nature* **448**, 714 (2007).
- M. Weber *et al.*, *Nat. Genet.* **39**, 457 (2007).
- R. Straussman *et al.*, *Nat. Struct. Mol. Biol.* **16**, 564 (2009).
- E. N. Gal-Yam *et al.*, *Proc. Natl. Acad. Sci. U.S.A.* **105**, 12979 (2008).
- A. M. Lindroth *et al.*, *PLoS Genet.* **4**, e1000145 (2008).
- S. Cao *et al.*, *Science* **298**, 1039 (2002); published online 26 September 2002 (10.1126/science.1076997).
- A. Smallwood, P. O. Estève, S. Pradhan, M. Carey, *Genes Dev.* **21**, 1169 (2007).
- K. Jepsen *et al.*, *Nature* **450**, 415 (2007).
- E. Viré *et al.*, *Nature* **439**, 871 (2006).
- M. Rush *et al.*, *Epigenetics* **4**, 404 (2009).
- K. D. Robertson, *Nat. Rev. Genet.* **6**, 597 (2005).
- We thank M. Carey (UCLA) for technical assistance on in vitro chromatin recruitment assays and J. Rubenstein (University of California San Francisco) for providing the pCAG-Dlx2 expression plasmid. This work was supported by NIH RO1 grants to Y.E.S. All microarray data are deposited in Gene Expression Omnibus (www.ncbi.nlm.nih.gov/geo/) under accession number GSE22476.

Supporting Online Material

www.sciencemag.org/cgi/content/full/329/5990/444/DC1
Materials and Methods
SOM Text
Figs. S1 to S18
Tables S1 and S2
References

5 April 2010; accepted 3 June 2010
10.1126/science.1190485

Functional Modules and Structural Basis of Conformational Coupling in Mitochondrial Complex I

Carola Hunte,^{1,2,3*} Volker Zickermann,^{4*} Ulrich Brandt^{4†}

Proton-pumping respiratory complex I is one of the largest and most complicated membrane protein complexes. Its function is critical for efficient energy supply in aerobic cells, and malfunctions are implicated in many neurodegenerative disorders. Here, we report an x-ray crystallographic analysis of mitochondrial complex I. The positions of all iron-sulfur clusters relative to the membrane arm were determined in the complete enzyme complex. The ubiquinone reduction site resides close to 30 angstroms above the membrane domain. The arrangement of functional modules suggests conformational coupling of redox chemistry with proton pumping and essentially excludes direct mechanisms. We suggest that a ~60-angstrom-long helical transmission element is critical for transducing conformational energy to proton-pumping elements in the distal module of the membrane arm.

Mitochondrial complex I [proton-pumping NADH (the reduced form of nicotinamide adenine dinucleotide):ubiquinone oxidoreductase] is a macromolecular membrane complex of close to one million daltons with a central function in energy metabolism (1). It is the entry point for electrons from NADH into the respiratory chain, and it couples electron transfer to ubiquinone with vectorial proton pumping across the inner mitochondrial membrane. With a stoichiometry of four protons to two electrons ($4\text{H}^+/2\text{e}^-$), it contributes about 40% of the proton motive force that drives adenosine 5'-triphosphate (ATP) syn-

thesis by ATP synthase (2, 3). Complex I is a source for deleterious reactive oxygen species (ROS) (4, 5) and has been implicated in the pathogenesis of a variety of neurodegenerative diseases such as Parkinson's disease, Alzheimer's disease, and Leigh syndrome (6, 7). Moreover, ROS generation by complex I may contribute to aging processes (8).

Despite the important physiological role of complex I, its molecular mechanism of energy conversion is essentially unknown. Progress in understanding complex I function has been severely limited by the lack of detailed structural information. Electron microscopy (EM) shows an L-shaped overall architecture with a membrane arm and a hydrophilic peripheral arm that protrudes into the mitochondrial matrix (9, 10) (Fig. 1A). The x-ray structure of the peripheral arm from a bacterial complex I was determined (11, 12).

The peripheral arm consists of two functional modules (I) and comprises all redox active cofactors (11). The N module contains the NADH oxidation site with one flavin mononucleotide (FMN) molecule as the primary electron acceptor, whereas the Q module contains the ubiquinone reduction site (Fig. 1A). Fast electron transfer between the two catalytic sites (13) is mediated by

a chain of seven iron-sulfur clusters. An additional iron-sulfur cluster localized near the FMN cofactor may serve a special function in protection against ROS formation (13–15). The membrane arm or P module harbors the proton-pumping machinery (16), presumably involving the three subunits—ND2, ND4, and ND5—that are homologous to sodium-proton antiporters (17).

Complex I is substituted by alternative enzymes in the widely used model organism *Saccharomyces cerevisiae*. Therefore, we have established the aerobic yeast *Yarrowia lipolytica* as a genetic model system to study eukaryotic complex I (18). In the complex from this source, 40 different subunits were identified with a total mass of 946.5 kD (19, 20). Fourteen central subunits are highly conserved among eukaryotes and prokaryotes (1). They form the structural core of the two arms of the complex and are essential for its bioenergetic functions. Twenty-six accessory subunits that are not found in prokaryotes are arranged around this core and presumably function in assembly, stabilization, regulation, and additional metabolic pathways that are not directly linked to energy conservation.

Here we report the x-ray crystallographic analysis of complete *Y. lipolytica* complex I (21). Phase information was obtained with anomalous data of a heavy atom cluster derivative and with native data (table S1). The molecule is L-shaped, with an angle between the two arms of about 100° (Fig. 1B). The membrane arm has a length of ~180 Å, and the distance between the tip of the peripheral arm and the bottom of the membrane arm is ~190 Å. At a resolution of 6.3 Å, many secondary structure elements and especially α -helical transmembrane segments were clearly recognized in the electron density.

The positions of all eight iron-sulfur cofactors were localized in the peripheral arm by anomalous Fourier analysis (Fig. 1B and table S1). The distances between the iron-sulfur clusters are similar to those reported for the hydrophilic fragment of bacterial complex I (15). Seven of these clusters constitute a continuous electron wire between the catalytic sites. Manual superimposition with the partial bacterial structure based on the

¹Institute for Biochemistry and Molecular Biology, Centre for Biological Signalling Studies (BIOS), University of Freiburg, D-79104 Freiburg, Germany. ²Institute of Membrane and Systems Biology, University of Leeds, Leeds LS2 9JT, UK. ³Department of Molecular Membrane Biology, Max Planck Institute of Biophysics, D-60438 Frankfurt am Main, Germany. ⁴Molecular Bioenergetics Group, Medical School, Cluster of Excellence Frankfurt "Macromolecular Complexes," Center for Membrane Proteomics, Goethe-University, D-60596 Frankfurt am Main, Germany.

*These authors contributed equally to this work.

†To whom correspondence should be addressed. E-mail: brandt@zbc.kgu.de



Supporting Online Material for

Dnmt3a-Dependent Nonpromoter DNA Methylation Facilitates Transcription of Neurogenic Genes

Hao Wu,* Volkan Coskun, Jifang Tao, Wei Xie, Weihong Ge, Kazuaki Yoshikawa, En
Li, Yi Zhang, Yi Eve Sun*

*To whom correspondence should be addressed. E-mail: ysun@mednet.ucla.edu (Y.E.S.);
haowu7@gmail.com (H.W.)

Published 23 July 2010, *Science* **329**, 444 (2010)
DOI: 10.1126/science.1190485

This PDF file includes:

Materials and Methods
SOM Text
Figs. S1 to S18
Tables S1 to S2
References

Supporting Online Material

Materials and Methods

Mouse postnatal SEZ/SVZ NSC culture

Postnatal day 14–21 day mouse lateral ventricle walls were dissected and mechanically dissociated as previously described (1). Single cell suspensions were plated at low density (10,000–20,000 cells cm⁻²) on cell culture dishes coated with poly-L-ornithine (PO)/fibronectin (FN), allowing individual cells to form spatially distinct colonies. Serial passage (less than 2 passages, or 2 weeks) allowed us to enrich undifferentiated NSCs to high purity (>95% Nestin⁺/Sox2⁺). The NSCs were maintained in serum-free B27 medium in presence of 10 ng/ml FGF-2/bFGF (Peprotech) and 10 ng/ml EGF (Invitrogen). The monolayer cultures were serially passaged every 4–7 days (up to 14 passages, 2 months) without losing their self-renewal ability and multipotency. To avoid the potential non-specific effect induced by culture adaption, only NSCs with limited *in vitro* culturing (less than 3 weeks) were used in the study. For tri-lineage differentiation, a cohort of undifferentiated NSCs, were re-plated on PO/FN substrate with mitogen for 2 days followed by withdrawal of mitogens for an additional 3 days. All animal experiments were done in accordance with the protocols approved by the Animal Research Committee of the University of California, Los Angeles.

Immunostaining

Cells on coverslip were fixed (4% paraformaldehyde (PFA) at room temperature), processed and stained (overnight at 4°C) for immunofluorescence analysis using following antibodies as previously described (2): mouse anti-Dnmt3a (1:400, Imgenex, C-terminus specific, for both Dnmt3a and Dnmt3a2), mouse anti-Dnmt3b (1:400, Imgenex, N-terminus specific, for all Dnmt3b isoforms), mouse anti-Map2 (1:1000, Sigma), mouse anti-Tubb3/TuJ1 (1:1000, Covance), mouse anti-CNPase/Cnp (1:400, Chemicon), mouse anti-Mbp (1:1000, Chemicon), rabbit anti-Nestin (1:1,000, a kind gift from Dr. Ron McKay at NINDS), goat anti-Sox2 (1:200, Santa Cruz), rabbit anti-Ki67 (1:1,000, Novocastra), anti-GFAP (guinea pig, 1:2,500, Advanced immunochemical; rabbit, 1:500, Chemicon), rabbit anti-H3K27me3 (1:1,000, Millipore), and rabbit anti-Ezh2 (1:1,000, Active Motif). Cy3-, Cy2- and Amca-conjugated donkey secondary antibodies were purchased from Jackson Immunoresearch. Hoechst 33342 dye was used to label the nuclei. Images were acquired on an Olympus fluorescent microscope.

Sagittal brain sections were prepared and processed for immunostaining as previously described (3) with minor modifications using following primary antibodies: rabbit anti-TuJ1 (1:1000, Covance), rabbit anti-Calbindin (1:100, Cell Signaling), sheep anti-TH (1:500, Pel-Freez), rabbit anti-Calretinin (1:500, Millipore), Guinea pig anti-Dcx (1:1,000, Millipore), guinea pig anti-Dlx2 (1:3,000) (4), anti-Sp8 (1:15,000, Millipore), rabbit anti-Ki67 (1:500, Novocastra), rabbit anti-GFAP (1:400, Millipore), mouse anti-Mbp (1:1,000, Millipore), rabbit anti-Dnmt3a (1:400, Santa Cruz), and rabbit anti-Dnmt3b (1:400, #157) (5). Briefly, wild-type and mutant mice (P21–24) were transcardially perfused by using 4% PFA. All brains were cryoprotected in 20% sucrose for 24 h, and cut in sagittal plane on a cryostat (Leica) at 10 µm. After several PBS washes, all slides were antigen-retrieved (95°C for 15min, Bio-Genex) and immersed in blocking solution (5% normal donkey serum and 0.2% Triton X-100 in PBS) for 1 h at room temperature. Primary antibody incubation was carried out overnight at 25°C with in dilution buffer (5% normal donkey serum and 0.5% Triton X-100 in PBS). The following day, slides were incubated with appropriate secondary antibodies as described above. The slides were examined by using Olympus fluorescent microscopes or a confocal system (Zeiss, LSM 510-META). Cell apoptosis in SVZ was examined using a Terminal deoxynucleotidyl transferase dUTP nick end labeling (TUNEL) kit (Roche).

Immunoblotting

The immunoblotting was performed essentially as described with minor modifications (6). Whole cell lysate were prepared from cells or tissues using SDS lysis buffer (1% SDS, 10 mM EDTA, 50 mM Tris-HCl, pH8.1) supplemented with protease inhibitor cocktails (Roche). The lysate was immediately sonicated using a microtip (Branson sonifier 450) to reduce viscosity. Protein concentration was measured by a BCA protein assay (Pierce). The cell lysates were stored at -80°C before use. 10–30 µg whole cell lysate was fractionated with 10% SDS-PAGE. The following mouse monoclonal antibodies were used: anti-Dnmt3a (1:250, C-terminus, Imgenex), anti-Dnmt3b (1:250, Imgenex), anti-Gapdh

(1:2,500, Abcam), and anti- β -actin (1:2,000, Sigma). The following rabbit polyclonal antibodies were used: anti-Dnmt3a (1:1,000, N-terminus, Santa Cruz), anti-Dnmt1 (1: 5,000, Path52, a kind gift from Dr. T. Bestor at Columbia University), anti-Suz12 (1:1,000, Abcam) and anti-Ezh2 (1:1,000, Active motif).

For immunoblotting of histone modifications, 10 μ g whole cell lysate was fractionated with 4-20% NuPAGE gel (Invitrogen) or 15% SDS-PAGE. The following polyclonal antibodies were used to probe histone modifications: anti-H3K4me3 (Millipore/Upstate, 07-473, or Abcam, ab8580), anti-H3K27me3 (Millipore/Upstate, 07-449), anti-H3K9me2 (Millipore/Upstate, 07-441, or Abcam, ab1220), anti-H3K9me3 (Abcam, ab8898), anti-H3K36me3 (Abcam, ab9050), anti-panH3 (Millipore/Upstate, 07-690).

RNA isolation and quantitative real-time RT-PCR

Total RNA was isolated using Trizol (Invitrogen). After Turbo DNase (Ambion) treatment, 1 μ g total RNA was used for cDNA synthesis using Superscript III (Invitrogen) following manufacturer's recommendations. Real-time PCR was performed in an iCycler using iQ SYBR Green Supermix (Bio-Rad). PCR efficiency and specificity of each primer pair was examined by standard curve of serially diluted cDNA and melting curve functionality respectively. Fold change was calculated based on $2^{-\Delta\Delta Ct}$ method after normalization to the transcript level of housekeeping gene *Gapdh*. Primer sequences used in the real-time RT-PCR are listed in the Table S2.

Gene expression microarrays

Two-color gene expression microarrays (Agilent) were used to directly compare relative changes in gene expression between WT and KO NSCs under proliferating or differentiation conditions. 500 ng of total RNA was labeled with Cy3- or Cy5-CTP using the Agilent Low RNA Input Fluorescent Linear Amplification Kit. After labeling and cRNA purification (Qiagen), cRNA was quantified using the NanoDrop spectrophotometer (Agilent). 825 ng Cy3- or Cy5-labelled cRNA were combined and hybridized to the Agilent 4x44K whole mouse genome microarray (G4122F, ~44,000 probes per array) for 17 h at 65 °C (10 r.p.m.). Replicate experiments were performed using biologically independent cultures with a dye-swap experimental design. Data was collected using Agilent microarray scanner and extracted using Feature Extraction 9.1 software (Agilent).

For identification of differentially expressed genes, we used NIA array analysis tool (<http://lgsun.grc.nia.nih.gov/ANOVA>). Of all the probes present on the microarray, signal intensity of redundant probes was averaged before analysis. Following parameters were used for analyzing statistically significant differential expression:

Threshold z-value to remove outliers: 10,000

Error Model: Max (Average, Bayesian)

Error variance averaging window: 200

Proportion of highest error variances to be removed: 0.01

Bayesian degrees of freedom: 5

False discovery rate (FDR) threshold: 0.05 (high stringency) or 0.2 (moderate stringency)

For clustering and heatmap display, Lowess-normalized signal intensity was log₂ transformed and median-centered. Heatmaps were generated using Cluster3 and Java Treeview.

Bisulphite conversion followed by genomic sequencing or MALDI-TOF MS

We carried out bisulfite conversion of 1 μ g Genomic DNA using EZ DNA methylation-Gold Kit (Zymo) according to manufacturer's instructions. Hot-start PCR was used to amplify the region of interest from the bisulfite converted genomic DNA. The PCR products were purified (Qiagen) and sub-cloned into the pCR4 TOPO vector (Invitrogen). 15-20 clones were randomly selected and sequenced using BigDye 3 terminator sequencing reagents (Applied Biosystems). Genomic sequences were retrieved from the UCSC genome database (mm8). All the bisulfite genomic sequencing primers were designed using the MethPrimer program. Primer sequences used in bisulfite genomic sequencing are listed in the Table S2.

Bisulphite conversion followed by Sequenom MassARRAY® MALDI-TOF Mass Spectrometry (MS) based quantitative DNA methylation analysis was performed in triplicate using standard protocol (Sequenom EpiTYPER DNA Methylation Analysis). The results were highly similar to those from bisulphite genomic sequencing analyses. Primers were designed using Sequenom's EpiDesigner tool (<http://www.epidesigner.com>). Primer sequences (without linker sequences) used in Sequenom analysis are listed in the Table S2. A T7-promoter tag is incorporated into each reverse PCR

amplification primer (5'-cagtaatacgactcactataggaga-3'), and a 10-mer linker sequence (5'-aggaagagag-3') is added to each forward primer that balances the primer length.

Chromatin immunoprecipitation (ChIP) and DNA tiling microarrays (ChIP-chip)

To immunoprecipitate chromatin, $2-5 \times 10^7$ (for Dnmt3a and PRC2 subunits, i.e. Suz12 and Ezh2) or $1-2 \times 10^7$ (for histone modifications) cells were cross-linked with 1% formaldehyde for 10 minutes at room temperature followed by exposure to 0.125 M glycine. After two washes with cold PBS, cells were collected as pellets and stored at -80°C before use. Nuclei were extracted and lysed sequentially with lysis buffer 1 (LB1, 50 mM Hepe2-KOH, pH7.5, 140 mM NaCl, 1 mM EDTA, 10% glycerol, 0.5% NP40, 0.25% Triton X-100), lysis buffer 2 (LB2, 10 mM Tris-HCl, pH8.0, 200 mM NaCl, 1 mM EDTA, 0.5 mM EGTA), and lysis buffer 3 (LB3, 10 mM Tris-HCl, pH8.0, 100 mM NaCl, 1 mM EDTA, 0.5 mM EGTA, 0.1% Na-Deoxycholate, 0.5% N-lauroylsarcosine). Chromatin was sonicated using a microtip (Branson sonifier 450) until the DNA fragments were reduced to 200-1000 bp in length. 10 μg antibodies were pre-incubated with 100 μl Dynal protein-G beads (Invitrogen) for at least 6 hours. Immunoprecipitation was performed overnight at 4°C with antibody conjugated protein-G beads. DNA/protein complexes were washed with RIPA buffer (50 mM Hepes-KOH, pH7.6, 500 mM LiCl, 1 mM EDTA, 1% NP-40, 0.7% Na-Deoxycholate) for 5 times and eluted from beads and reverse cross-linked at 65°C overnight. The DNA was digested with RNase A and proteinase K sequentially, followed by phenol/chloroform extraction ethanol precipitation. Following antibodies were used in ChIP assays: anti-H3K4me3 (ab8580, Abcam or 07-473, Millipore), anti-H3K27me3 (07-449, Millipore), anti-panH3 (07-690, Millipore), anti-Dnmt3a (Santa Cruz), anti-Ezh2 (39103, Active Motif), and anti-Suz12 (a kind gift from Dr. Y. Zhang).

Real-time quantitative PCR was performed in an iCycler using iQ SYBR Green Supermix (Bio-Rad). For quantification of relative level of Dnmt3a, PRC2 and histone modification occupancy, we calculated the percentage of immunoprecipitated DNA over input DNA. Primer sequences used in ChIP-qPCR are listed in the Table S2.

For whole-genome DNA tiling microarray analyses of Dnmt3a (in WT, IP/WCE) and H3K27me3 (WT versus KO, IP/IP) occupancy, we amplified ChIP or input DNA samples using whole genome amplification kit (Sigma). Amplified ChIP or input samples were labeled (5' Cy5- or Cy3-random nonamers, TriLink Biotechnologies) using the standard protocol (NimbleGen Arrays User's Guide for ChIP-chip analysis). Hybridization of labeled samples to whole genome HD2 microarrays 4-array set (Roche/NimbleGen, ~ 2.1 million tiling probes per array, covering the entire non-repetitive portion of mouse genome) was carried out for 16-20 h at 42°C using NimbleGen hybridization System 4. After stringent washes, microarrays were subsequently scanned using the Agilent scanner at 5 micron resolution. Data were extracted and analyzed using NimbleScan v2.5 (Roche/NimbleGen). Dnmt3a binding sites were identified by a sliding window-base statistical algorithm in NimbleScan v2.5 (FDR < 1% or < 5%). For identification of probes associated with significant increase in H3K27me3 levels in KO NSCs as compared to WT NSCs, a non-parametric one-sided Kolmogorov-Smirno (KS) test was used (KS score > 2). Briefly, from the scaled log₂-ratio data, a fixed-length window (750bp) is placed around each consecutive probe and the one-sided KS test is applied to determine whether the probes are drawn from a significantly more positive distribution of intensity log-ratios than those in the rest of the array. The resulting score for each probe is the $-\log_{10}$ P-value from the windowed KS test around that probe. Using NimbleScan v2.5, peak data files are generated from the P-value data files. NimbleScan software detects peaks by searching for at least 2 probes above a P-value minimum cutoff ($-\log_{10}$) of 2. Peaks within 500bp of each other are merged.

For extended promoter tiling microarray analyses of Dnmt3a, PRC2 (Suz12 and Ezh2) and histone modification (H3K4me3, H3K27me3 and histone H3) occupancy, we amplified input and ChIP DNA samples using two-step ligation-mediated PCR (LM-PCR) as previously described (7) or whole genome amplification kit (Sigma). For hybridization with mouse extended promoter tiling microarray 2-array set (Agilent, G4490A, $\sim 244,000$ probes per array, ~ 280 bp per probe, covering approximately -5.5kb to +2.5kb genomic regions relative to TSS of $\sim 17,000$ annotated Refseq genes), 2 μg of amplified input and IP DNA was labeled with Cy3- and Cy5-dUTP (Perkin Elmer) respectively using Bioprimer DNA labeling System (Invitrogen). For direct comparison of chromatin immunoprecipitated from wild-type and *Dnmt3a*-deficient NSCs, WT and KO samples were labeled with Cy3- and Cy5-dUTP respectively. Hybridization was carried out for 40 h at 65°C (10-15 r.p.m.) and subsequently scanned using an Agilent scanner. Data were extracted using Feature Extraction 9.1 (Agilent) and analyzed using ChIP analytics 1.3 (Agilent). For IP versus WCE (IP/WCE) comparison, we performed blank subtraction normalization,

inter-array median normalization and intra-array (dye-bias) median normalization by calculating a one-step Tukey biweight median before peak detection. For IP versus IP (IP/IP) comparison, we performed an intra-array Lowess (intensity-dependent) normalization. Two Dnmt3a ChIP-chip experiments using biological independent samples were performed and yielded highly reproducible results. We combined and processed the replicate array results to identify Dnmt3a high affinity targets. Probes associated with significant level of Dnmt3a signals were called on the basis of a built-in heuristic algorithm ($P_{\bar{x}} < 0.001$) incorporating neighbor probes information using a Whitehead error model (Agilent ChIP analytics 1.3). Probes associated with significant level of histone modification signals were also called on the basis of the built-in heuristic algorithm ($P_{\bar{x}} < 0.002$ for H3K27me3 or $P_{\bar{x}} < 0.2$ for H3K4me3) (Agilent ChIP analytics 1.3). This statistical method generated highly similar lists of genes associated with given histone modification within promoter regions as compared to that of previously reported in NSCs using ChIP-seq method (8). For visualization, raw enrichment ratios of annotated probes (UCSC, mm7) were displayed as bar graph (log2 ratios). Moreover, IP/WCE comparison and IP/IP comparison of WT and KO samples generated highly similar results.

For calculating the averaged enrichment distribution of unprocessed probe signals (log2 Ratio), Dnmt3a binding sites or regions associated with significant changes in H3K27me3 levels data were binned to 500-bp intervals using a 250-bp sliding window within genomic regions (10-bk for NimbleGen whole-genome microarrays, 2.5kb for Agilent extended promoter microarrays) flanking TSSs of annotated Refseq genes. Heatmaps were generated and visualized using Cluster3 and Java Treeview, respectively.

Methylated DNA immunoprecipitation (MeDIP) and DNA tiling microarrays (MeDIP-chip)

MeDIP assay was carried out as previously described with minor modifications (9). Briefly, genomic DNA was digested with proteinase K and RNase A sequentially, and purified by phenol/chloroform extraction. Purified genomic DNA was sonicated and heat-denatured (95 °C, 10 min). An aliquot of sonicated genomic DNA was saved as input. 5 µg fragmented genomic DNA was immunoprecipitated with 5 µl of monoclonal antibody against 5-methylcytidine (Eurogentec) at 4 °C overnight in a final volume of 500 µl of IP buffer (10 mM sodium phosphate (pH 7.0), 140 mM NaCl, 0.05% Triton X-100). We incubated the DNA-antibody mixture with 30 µl protein G Dynabeads (Invitrogen) for 2 h at 4 °C and washed it three times with 1 ml IP buffer. We then treated the beads with proteinase K for at least 3 h at 55 °C and purified the methylated DNA by phenol-chloroform extraction followed by ethanol precipitation. For real-time PCR analysis, 10 ng of input genomic DNA and 1/30 of the immunoprecipitated (IP) methylated DNA was used for each PCR reaction. MeDIP-qPCR was performed in an iCycler (Bio-Rad) using iQ SYBR Green Supermix (Bio-Rad). Reactions were done in duplicates and standard curves were calculated on serial dilutions of input genomic DNA. ChIP primers were used in MeDIP-qPCR to quantify the relative DNA methylation level within the regions occupied by Dnmt3a.

For microarray analyses, we amplified input and immunoprecipitated DNA using whole genome amplification kit (Sigma). Labeling, hybridization, array processing and data extraction were done following procedures described for ChIP-chip. Data analysis was performed using ChIP analytics 1.3 (Agilent, for extended promoter microarrays) or NimbleScan v2.5 (Roche/NimbleGen, for whole-genome microarrays). For identification of probes associated with significant decrease in DNA methylation levels in KO NSCs as compared to WT NSCs, a non-parametric one-sided Kolmogorov-Smirno (KS) test was used.

Lentiviral infection and acute ablation of Dnmt3a in *Dnmt3a^{flx/flx}* NSCs

Control (UbiC-empty-IRES-EGFP) or Cre-expressing (UbiC-Cre-IRES-EGFP) FUIGW lentiviral vector was co-transfected with three other helper vectors (VSVG, RSV-REV and pMDL g/p RRE) into HEK-293T cells as previously described (<http://www.sciencegateway.org/protocols/lentivirues/index.htm>). Packaged lentiviral particles were harvested at 48h and 72h post transfection. Harvested lentiviral particles were then combined and concentrated using ultracentrifugation (Beckman SW28 rotor, 25,000 rpm for 90 min). The embryonic or postnatal *Dnmt3a^{flx/flx}* NSCs were transduced with concentrated control or Cre-expressing lentiviruses in presence of 4 µg/ml polybrene (Sigma) in two consecutive days and analyzed 5 days after first infection. The typical infection efficiency of NSCs was 40-60% 3 days after first infection based on EGFP fluorescence. Depletion of Dnmt3a after infection was routinely monitored by immunostaining of EGFP, Cre and Dnmt3a.

Short-hairpin RNA (shRNA)-mediated suppression of PRC2 core subunits in *Dnmt3a*-null NSCs

A lentiviral vector encoding shRNA specific for Suz12 (NM_199196, Sigma MISSION™ TRC shRNA set) was used for silencing Suz12 expression (TRCN0000123889, targeting 3' UTR, 5'-CCGGGCTGTCTTAGAGATGGAGAATCTCGAGATTCTCCATCTCCATCTCTAAGACAGCTTTTTTG-3'). Two lentiviral vectors encoding shRNA specific for Eed (NM_021876, Sigma MISSION™ TRC shRNA set) were used for inhibiting Eed expression (#1: TRCN0000095719, targeting 3' UTR, 5'-CCGGTCTTGCTAGTAAGGGCACATACTCGAGTATGTGCCCTTACTAGCAAGATTTTTG-3'; #2: TRCN0000095722, targeting CDS, 5'- CCGGGAAGCAACAGAGTAACCTTATCTCGAGATAAGGTTACTCTGTTGCTTCTTTTTG-3'). A control shRNA vector (SHC002, The MISSION™ Non-Target shRNA Control Vector, Sigma), which contains a shRNA sequence that does not target human and mouse genes (>4 base pair mismatches to any known human or mouse gene), was used as a negative control for Suz12 and Eed knockdown shRNAs. Lentiviruses were packaged as described above and were used for infecting NSCs in presence of 4 µg/ml polybrene (Sigma). NSCs were infected for two consecutive days and subsequently selected in media containing 2 µg/ml puromycin for 7-10 days before analysis.

Re-expression of WT or catalytically inactive *Dnmt3a* in *Dnmt3a*-null NSCs

Dnmt3a-null NSCs were transfected with the control vector (CAG-empty-IRES-blasticidin) and expression vectors encoding catalytically active (CAG-*Dnmt3a*^{WT}-IRES-blasticidin) or catalytically inactive (CAG-*Dnmt3a*^{P705V/C706D}-IRES-blasticidin) *de novo* DNA methyltransferases using lipofectamine 2000 (Invitrogen) according to manufacturer's recommendations. As a control, wild-type NSCs were also transfected with the empty vector (CAG-empty-IRES-blasticidin). After 24 h, transfected NSCs were passaged and subsequently selected in 5 µg/ml blasticidin-containing medium for 8-10 days before analysis.

***In vitro* chromatin recruitment assay**

A 1.1kb genomic region corresponding to *Dnmt3a* bound regions within the *Dlx2* gene was PCR cloned, purified and biotinylated at one terminus (a NotI site) by Klenow filling reactions. An aliquot of DNA was *in vitro* methylated by the CpG DNA methylase, SssI (NEB) following manufacturer's instructions. Both methylated and unmethylated DNA was then assembled into chromatin arrays consisted of recombinant *Xenopus* histones using salt dialysis as previously described (10). After immobilization using streptavidin-conjugated magnetic beads (Invitrogen), chromatin arrays were then incubated with *in vitro* reconstituted PRC2 complexes (Ezh2, Eed, Suz12, Aebp2, and RbAp48) for 30 min with rotation at room temperature (11). After several washes with binding buffer, the beads and bound PRC2 complexes were re-suspended in SDS sampling buffer and fractionated by 10% or 15% SDS-PAGE. The bound fraction of PRC2 complexes was detected by western blotting. The following primers were used to clone the 1.1kb genomic fragment within the *Dlx2* gene: forward 5'- CCACATCTTCTTGAACCTTGGATCG-3'; reverse 5'- GTAAGCATCGCAAGCATCTAGGG-3'.

Supporting Text

Gene expression analysis of differentiating WT and KO SEZ/SVZ NSC cultures

To further investigate the effect of Dnmt3a on cell fate specification during postnatal NSC differentiation, we performed expression profiling of differentiating NSCs and cross-referenced the datasets with a published database where cell-type specific gene expression was comprehensively examined in highly enriched postnatal neuronal and glial populations (12). Among 766 down-regulated genes in differentiating KO cells, the percentage of neuronal genes was significantly enriched in down-regulated genes (32.1% versus 11.7% expected by chance, $P=3.34 \times 10^{-48}$), but not in up-regulated genes (8.5%). GO analysis also confirmed that genes functionally related to neurogenesis were overly represented in genes down-regulated in differentiating KO cells (Table S1). In contrast, glial lineage genes showed an opposite trend (25.5% in down-regulated genes; 46.3% in up-regulated genes), and were only enriched in up-regulated genes ($P=3.58 \times 10^{-39}$), indicating that Dnmt3a may also be involved in regulating glial lineage differentiation. Indeed, several Dnmt3a targets critically involved in astroglial (e.g. *Gfap* and *S100b*) and oligodendroglial differentiation (e.g. *Nkx2-2*, *Pdgfra* and *Mbp*) were significantly up-regulated in differentiating KO cultures. Taken together, these findings support the hypothesis that Dnmt3a is involved in maintaining neurogenic potential in postnatal NSCs by directly promoting transcription of neurogenic targets while repressing differentiation genes of alternative glial lineages through different mechanisms.

Mechanisms of Dnmt3a-dependent gene activation

Although we cannot entirely exclude the possibility that *Dnmt3a*-deficiency may induce a transcriptional repressor, which in turn represses other genes including some Dnmt3a targets, this seems unlikely, because we did not find a known repressor in the list of up-regulated genes in KO NSCs. Furthermore, all the Dnmts may possess methyltransferase activity independent functions in developmental gene regulation. In our rescue experiments, catalytically inactive Dnmt3a mutant re-occupy most, if not all, Dnmt3a binding-sites, but fail to restore normal chromatin states (reduce aberrantly elevated PRC2/H3K27me3 levels at H3K4me3-high/CpG-rich Dnmt3a targets) and neurogenesis deficits in *Dnmt3a*-null postnatal NSCs. Thus, DNA methylation independent functions of Dnmts are unlikely to play a major role in the gene regulatory events described in our study.

Non-promoter DNA methylation and gene expression in other tissues

While we have focused our epigenomic analyses on postnatal SEZ/SVZ neural stem cells (NSCs), multiple lines of evidence suggest that the positive correlation between non-promoter DNA methylation and tissue-specific gene expression is not restricted to this system. First, partial inactivation of maintenance methyltransferase Dnmt1 in other lineage-committed stem/progenitor cells (blood or skin) via hypomorphic mutations or lentiviral shRNA inhibition results in similar number of genes that are up-regulated or down-regulated (13, 14). Second, previous efforts on identifying tissue-specific de novo DNA methylated regions in human adult tissues have also revealed a strong positive correlation between non-promoter methylation (i.e. intragenic DNA methylation) and tissue-specific transcription of a cohort of developmentally regulated genes, including genes (e.g. PAX6 and UNC13A) specifically expressed in brain tissues (15). Third, unbiased genome-wide analyses indicate that high levels of DNA methylation are found in gene bodies of transcriptionally active genes in both human fibroblasts and B-cells (16, 17). Finally, gene body DNA methylation is a widespread phenomenon on actively transcribed X-chromosome, whereas promoter DNA methylation, but not intragenic methylation is present on the inactive X-chromosome in female cells (18).

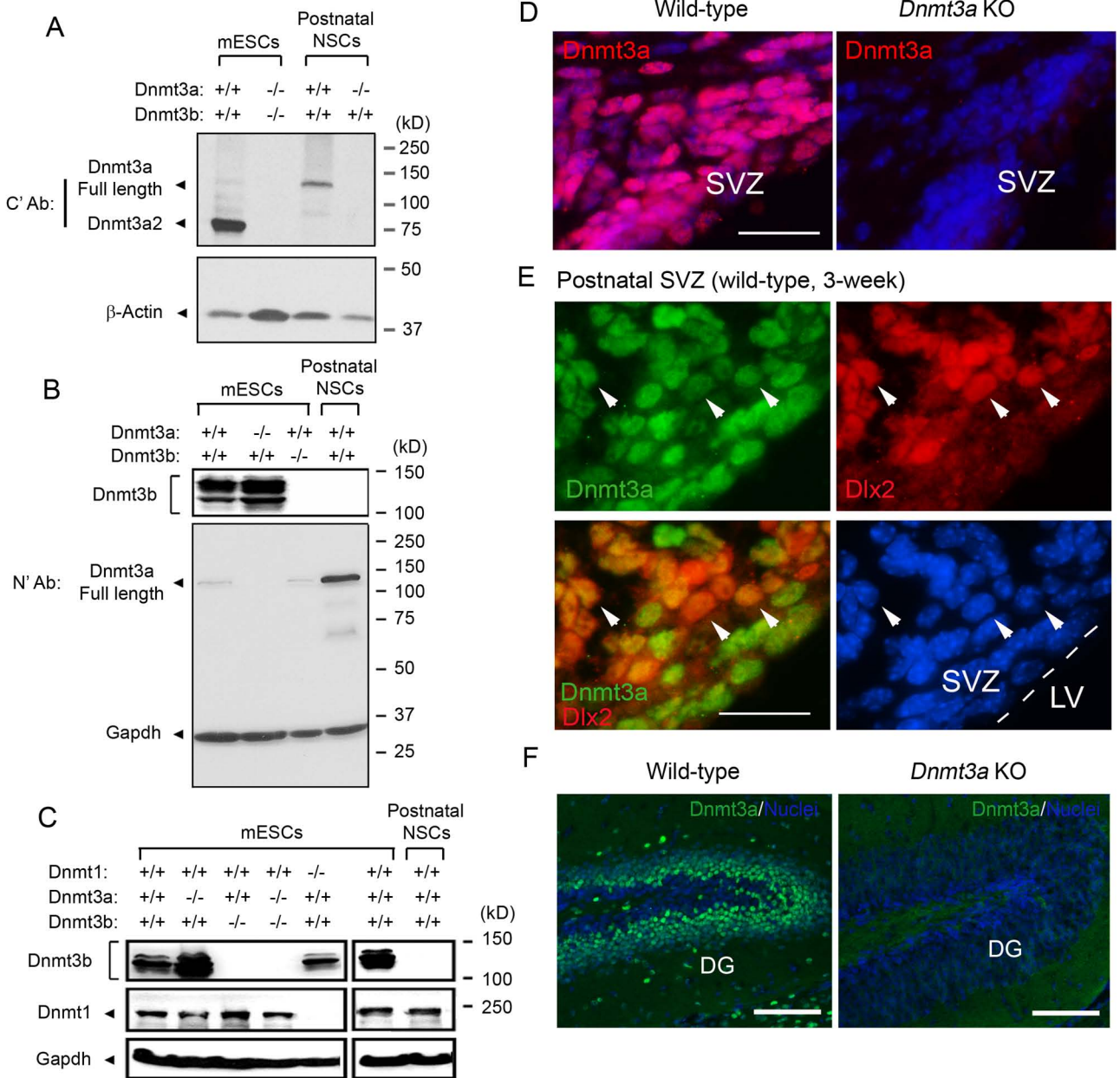


Fig. S1 Dnmt3a expression in embryonic stem cells (ESCs), postnatal neural stem cells (NSCs) and postnatal neurogenic zones.

(A-B) Immunoblotting using antibodies against Dnmt3a in ESCs and postnatal subventricular zone (SVZ) NSCs. The anti-Dnmt3a C-terminus monoclonal antibody (C' Ab in A) recognizes both full-length Dnmt3a (~130kD) and N' truncated Dnmt3a2 variant (~75kD). N' specific polyclonal antibodies (N' Ab in B) only recognize the full length Dnmt3a.

(C) Immunoblotting using antibodies against Dnmt3b and Dnmt1 in ESCs and NSCs with indicated genotypes.

(D) Immunohistochemistry for Dnmt3a (red) in subventricular zone (SVZ) sagittal brain sections of wild-type and *Dnmt3a*-null mice. Scale bars, 25 μm.

(E) Immunohistochemistry for Dnmt3a (green) and the neuronal progenitor marker Dlx2 (red) in sagittal brain sections of wild-type mice. Arrow heads indicate cells expressing both Dlx2 and Dnmt3a. Scale bars, 25 μm.

(F) Representative immunofluorescence images of Dnmt3a in WT and KO dentate gyrus (DG) at postnatal 3-weeks. Scale bar, 100 μm.

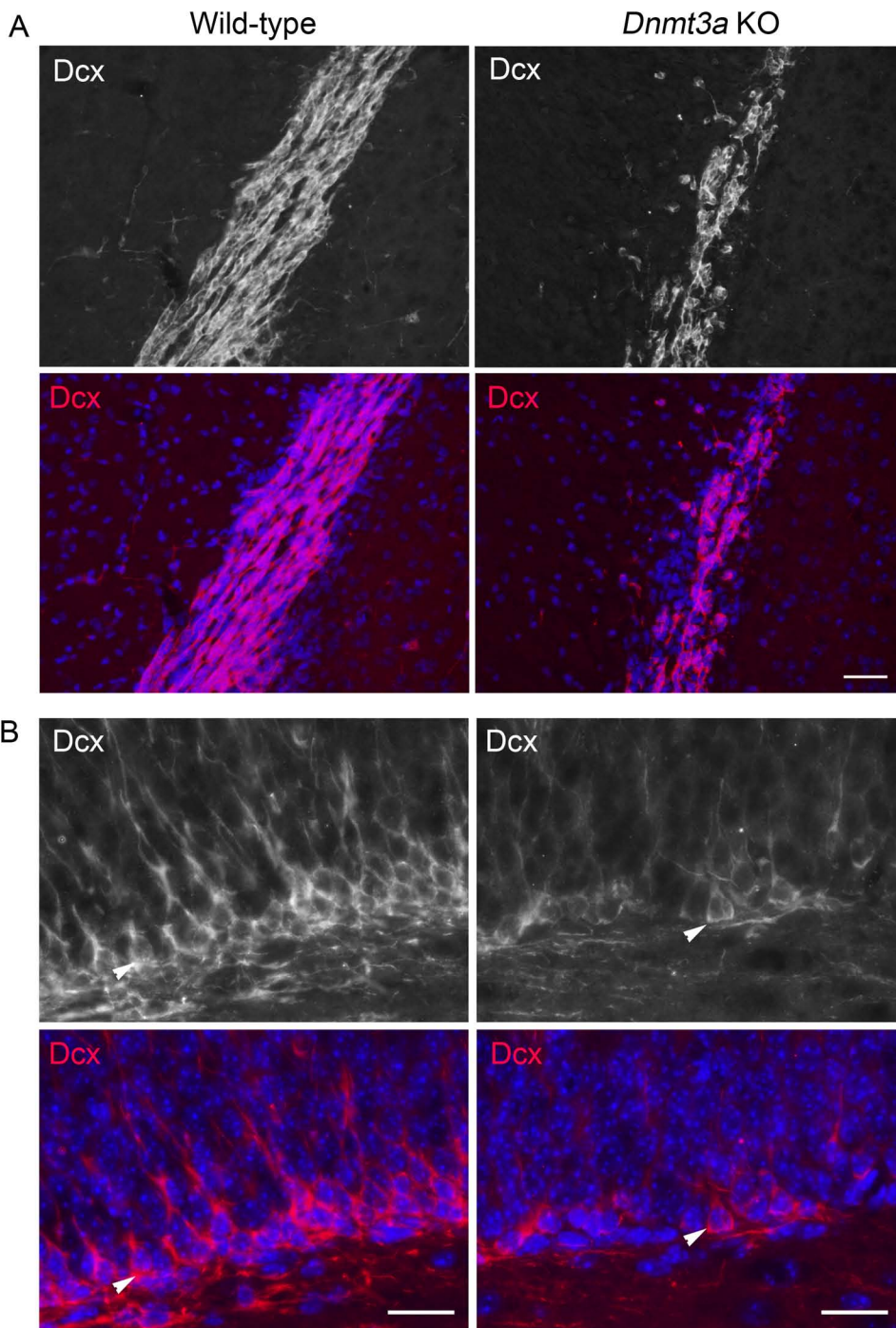


Fig. S2 *Dnmt3a*-deficiency impairs postnatal subventricular zone (SVZ) and hippocampal dentate gyrus (DG) neurogenesis.

(A) Immunohistochemistry for the neuroblast marker Dcx in SVZ sagittal brain sections of WT and KO mice at postnatal 3 weeks. Quantification of Dcx in SVZ is present in Fig. 1B. Scale bars, 50 μ m.

(B) Representative immunostaining of the immature neuronal marker Dcx in WT and KO postnatal (3-weeks) DG (36 \pm 3.3 Dcx+ cells per section in WT versus 25 \pm 4.3 in KO, mean \pm s.d.; $P < 0.05$).

Arrow heads indicate Dcx+ cells. Scale bar, 50 μ m.

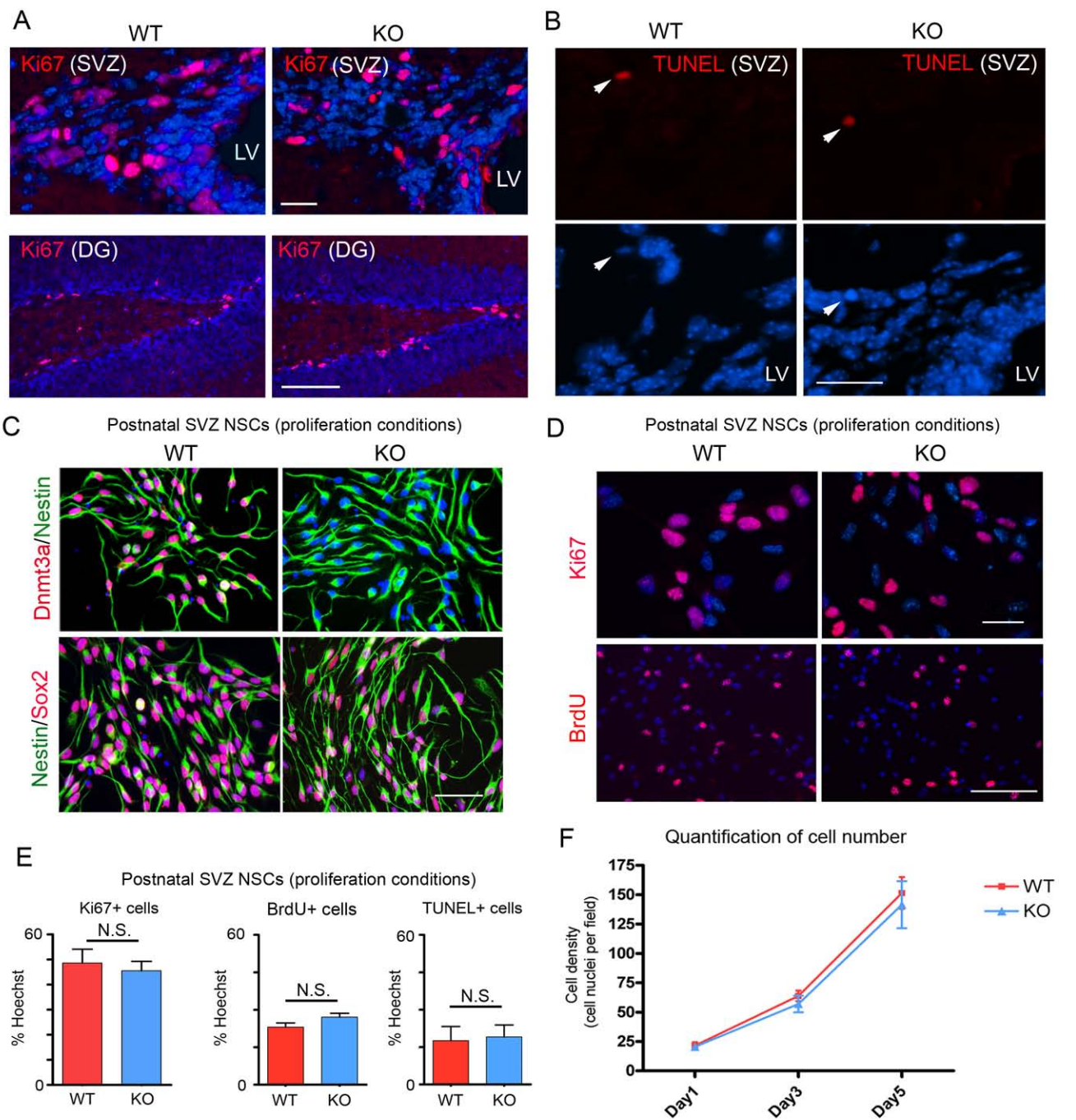


Fig. S3 Dnmt3a is dispensible for proliferation, survival and maintenance of undifferentiated states of postnatal NSCs.

(A) No significant difference in number of Ki67+ proliferating cells was observed between WT and KO at both SVZ (82% of WT, 21% s.d.) and DG (96% of WT, 29% s.d.). Scale bars, 20 μ m (SVZ) or 100 μ m (DG).

(B) TUNEL assay in SVZ sagittal brain sections of WT and KO mice. Scale bars, 20 μ m.

(C) Immunostainings of NSC markers Nestin and/or Sox2 in WT and KO NSCs showed that most of Dnmt3a-null NSCs (>90%) were still in undifferentiated states. Scale bars, 50 μ m.

(D) Immunostaining of Ki67 and 5-Bromo-2-deoxyuridine (exposed to BrdU for 2h before analysis) in WT and KO SVZ NSC cultures at day 3 after passaging. Scale bar, 20 (upper) or 100 (lower) μ m.

(E) Quantification of proliferation and cell death rate in WT and KO SVZ NSCs. Error bars, s.e.m. of triplicate experiments.

(F) Quantification of the cell growth in WT and KO SVZ NSC cultures at day 1, 3 and 5 after plating.

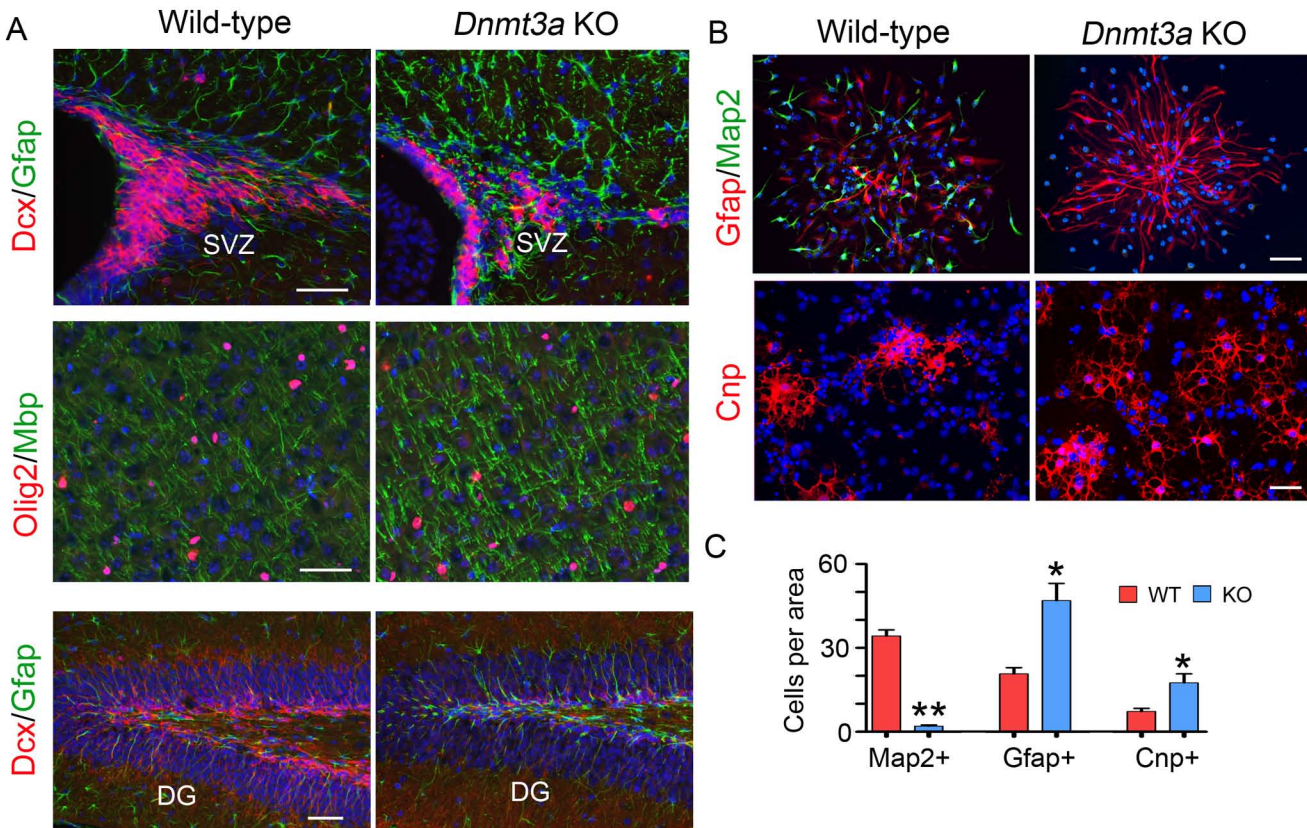


Fig. S4 Dnmt3a is dispensible for postnatal gliogenesis in vivo and in SVZ NSC cultures.

(A) Immunohistochemistry for the neuroblast marker Dcx, the astroglial marker Gfap and oligodendroglial markers Olig2 as well as Mbp in sagittal brain sections of WT and KO mice at P24. Shown for Olig2 and Mbp immunostaining are cortical regions immediately above corpus callosum (CC). Scale bars, 50 μ m.

(B) Immunocytochemistry for the neuronal marker Map2, the astroglial marker Gfap and the oligodendroglial marker CNPase/Cnp in differentiating WT and KO SVZ NSC cultures. Scale bars, 50 μ m.

(C) Quantification of the number of Map2⁺ neurons, Gfap⁺ astrocytes and Cnp⁺ oligodendrocytes after 3 days of differentiation. Error bars, s.e.m. (*, $P < 0.05$; **, $P < 0.01$; $n = 4$).

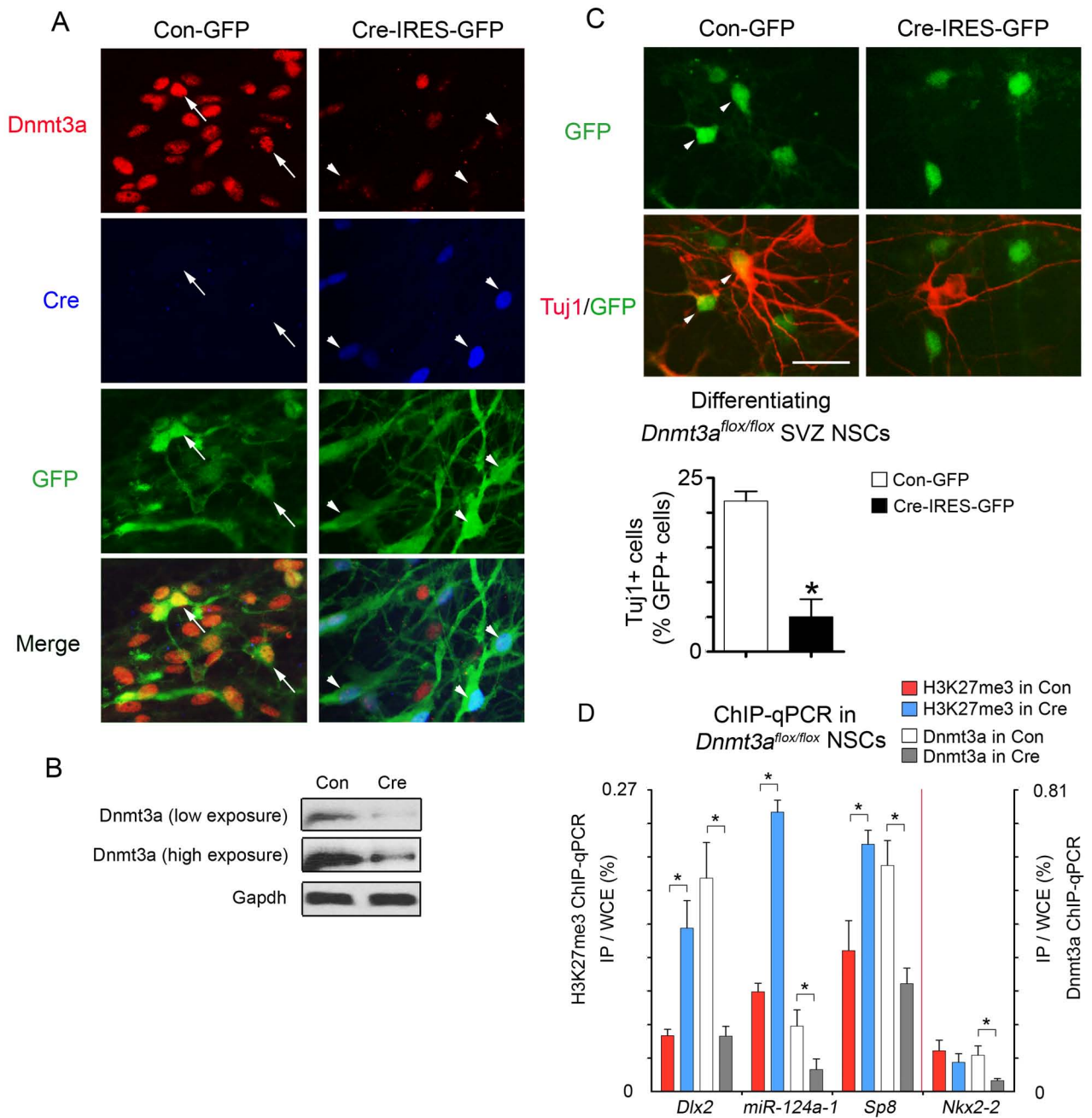


Fig. S5 Cre recombinase mediated acute ablation of Dnmt3a in *Dnmt3a^{flox/flox}* NSCs impairs neurogenesis and causes aberrant increase in H3K27me3 on neurogenic targets.

(A-B) Immunostaining (A) and western blotting (B) of Dnmt3a expression levels in postnatal *Dnmt3a^{flox/flox}* NSCs infected with control (empty-IRES-GFP) and Cre (Cre-IRES-GFP) lentiviruses for 5 days before analysis. Arrow (left) and arrowhead (right) in (A) marked GFP-positive cells in con- and Cre-lentivirus infected *Dnmt3a^{flox/flox}* NSCs. Gapdh was used in (B) as a loading control.

(C) Tuj1+GFP+ double-positive cells were significantly fewer in *Dnmt3a^{flox/flox}* NSCs infected with Cre lentiviruses than those infected with control. Error bars, s.e.m. (*, as compared to control infected cells, $P < 0.005$, $n = 3$). Scale bar, 20 μm .

(D) Dnmt3a occupancy and H3K27me3 levels of 4 representative Dnmt3a target genes were determined by ChIP-qPCR in control and Cre lentivirus infected postnatal NSCs (*, as compared to WT, $P < 0.01$, $n = 3$). Error bars represent s.e.m. determined from three independent experiments.

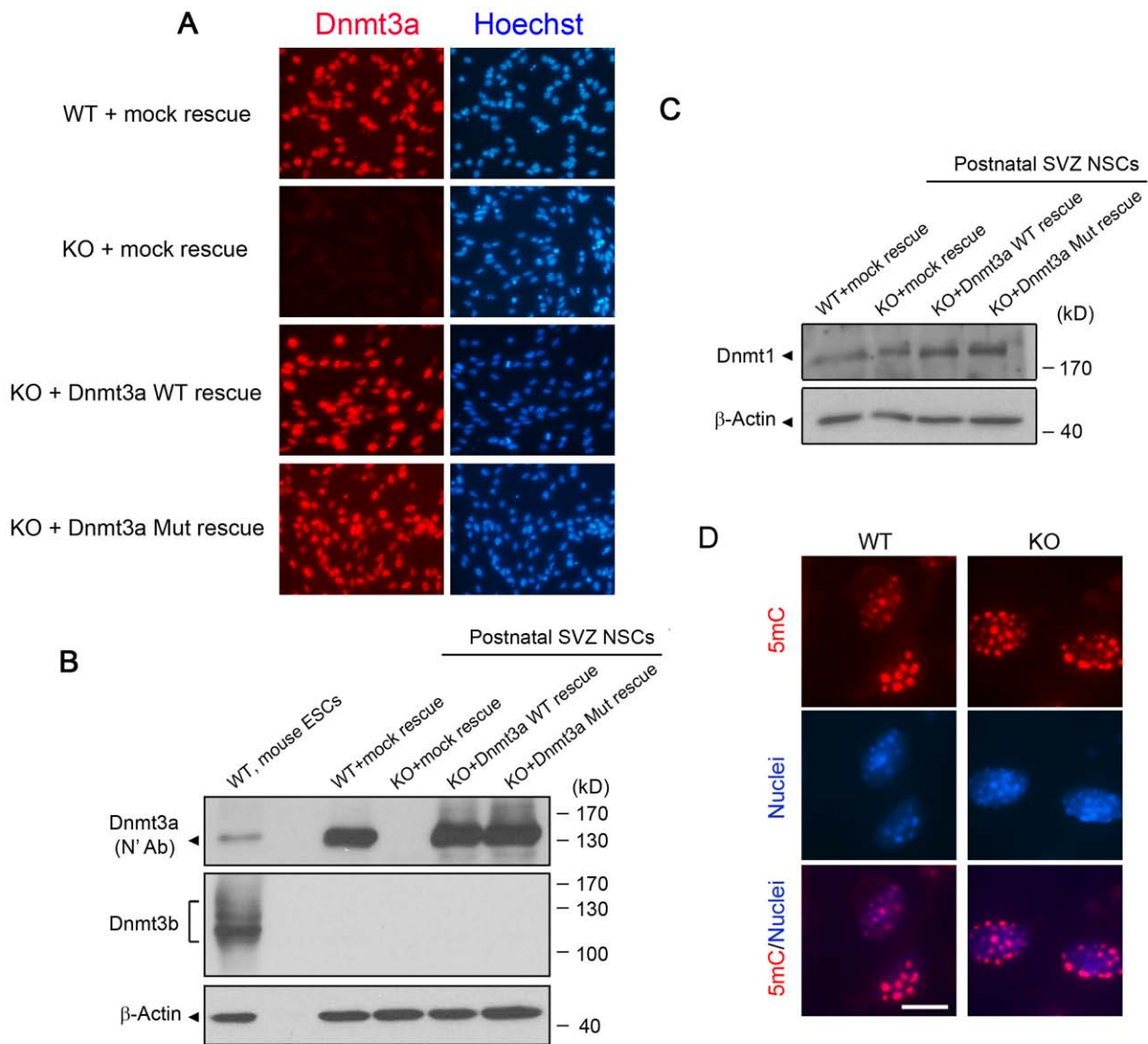


Fig. S6 *Dnmt3a*-deficiency does not alter expression of other DNA methyltransferases (*Dnmt3b* and *Dnmt1*) and global DNA methylation patterns in postnatal NSCs.

(A) Immunostaining of *Dnmt3a* in WT, KO and rescued NSCs.

(B) Immunoblotting analysis of de novo DNA methyltransferases, *Dnmt3a* and *Dnmt3b*, in WT, KO and rescued SVZ NSCs. Whole cell lysate from mouse ESCs were used as a positive control for *Dnmt3b* proteins, which are undetectable in postnatal SVZ NSCs.

(C) Comparable expression levels of *Dnmt1* are detected in WT, KO and rescued SVZ NSCs.

(D) Global DNA methylation pattern is not altered in KO NSCs as measured by immunostaining of 5-methylcytosine (5mC) in WT and KO postnatal SVZ NSCs. Nuclear punctate loci that are highlighted by Hoechst 33342 likely represent regions enriched with hypermethylated repetitive DNA sequences. Scale bar, 10 μ m.

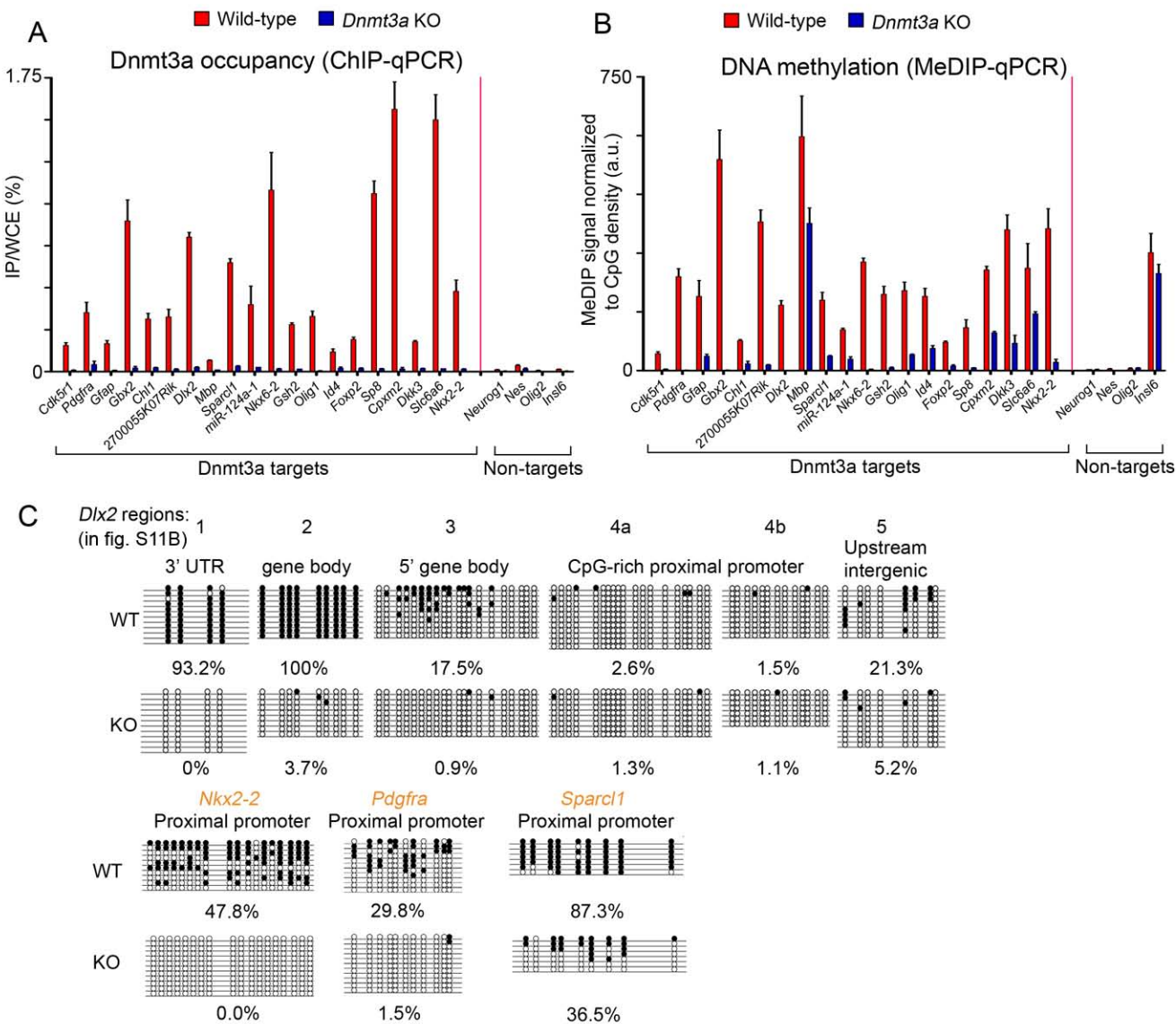


Fig. S7 Locus-specific validation of Dnmt3a ChIP-chip and MeDIP-chip.

(A-B) Quantitative PCR (qPCR) validation of Dnmt3a occupancy (A) and DNA methylation (B) for Dnmt3a bound ($n=20$) and unbound ($n=4$) genes in WT and KO NSCs. The MeDIP-qPCR signals (IP/Input, %) are normalized to CpG-density (CpG-per-bp) of PCR amplicon and flanking genomic regions (200bp, up- and down-stream) and normalized DNA methylation levels are shown as arbitrary units (a.u.).

(C) Bisulphite sequencing analyses of selected genomic regions in wild-type (WT) and *Dnmt3a*-null (KO) NSCs. Methylated (filled circles) and unmethylated (open circles) CpG dinucleotides are shown for multiple independently sequenced alleles (horizontal lines). Methylation level is quantified as the percentage of methylated over total CpGs. Results were pooled from two independent NSC cultures.

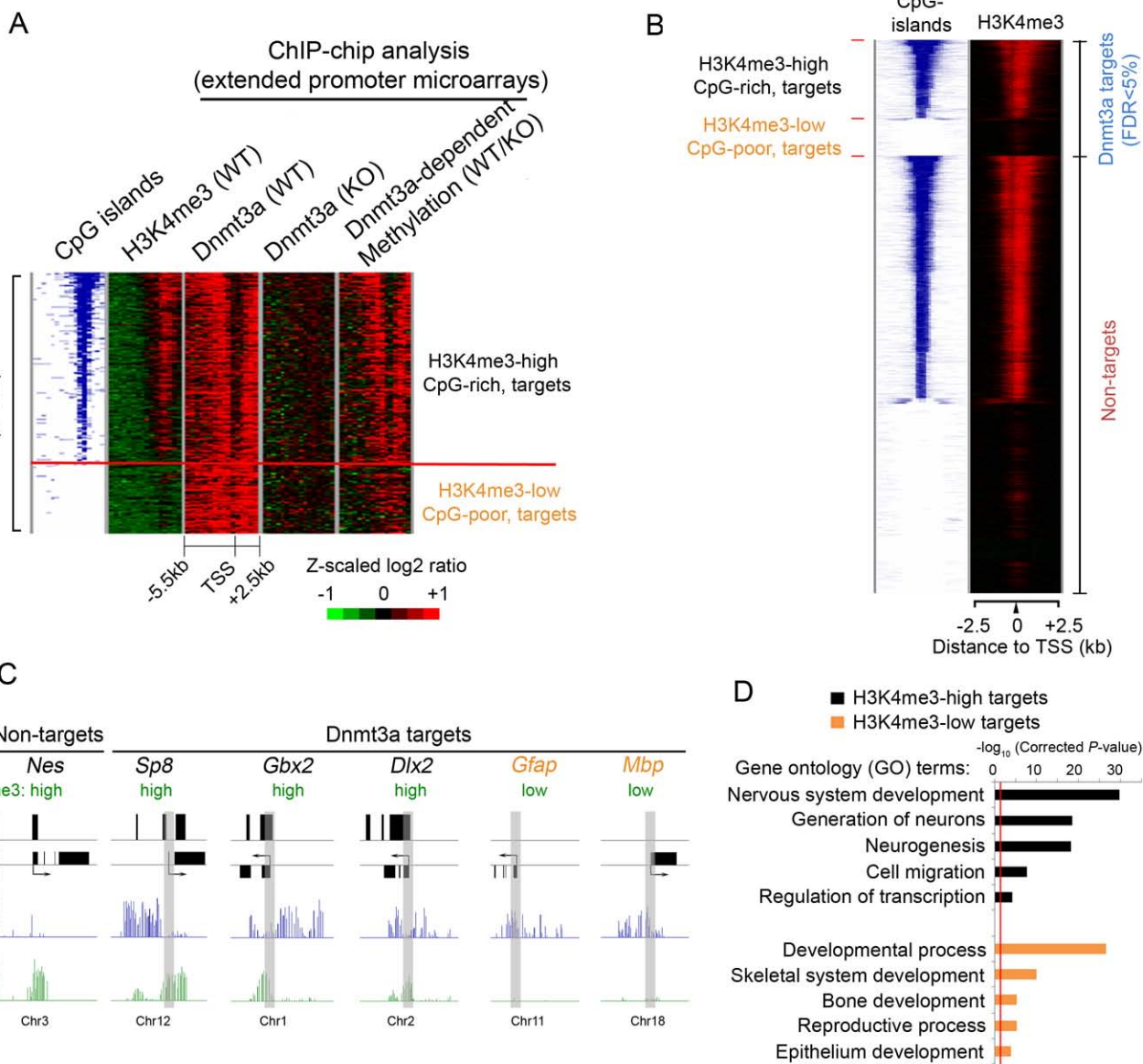


Fig. S8 Genomic analysis of Dnmt3a occupancy and H3K4me3 within extended promoters in SVZ NSCs. (A) ChIP-chip analysis using extended promoter microarrays (-5.5kb to +2.5kb) of Dnmt3a (IP/WCE in WT and KO), H3K4me3 (IP/WCE in WT) and Dnmt3a-dependent DNA methylation (IP/IP, WT/KO). Note that 87.4% of Dnmt3a targets identified by extended promoter arrays are also found in the Dnmt3a target list generated from whole-genome experiment, and the specific Dnmt3a binding sites in WT NSCs is absent in *Dnmt3a*-null NSCs. Heatmap representation are shown for Dnmt3a targets identified by extended promoter DNA microarray, and the relative enrichment for normalized ChIP-chip signals are represented by color intensity. Dnmt3a targets were ranked by the CpG-density of CpG-islands within -2.5kb to +2.5kb promoter regions. (B) The transcriptionally permissive histone mark H3K4me3 is highly enriched on CpG-rich gene promoters. (C) Relative spatial distribution of CpG-islands, Dnmt3a and H3K4me3 within representative Dnmt3a targets with CpG-rich and CpG-poor promoters. Regions shaded in gray indicate 1-kb core promoter regions (-0.5kb to +0.5kb). A non-target, the NSC marker gene *Nes*/*Nestin*, is shown as a control. (D) Gene ontology (GO) analysis of CpG-rich/H3K4me3high (black) and CpG-poor/H3K4me3low (orange) Dnmt3a targets.

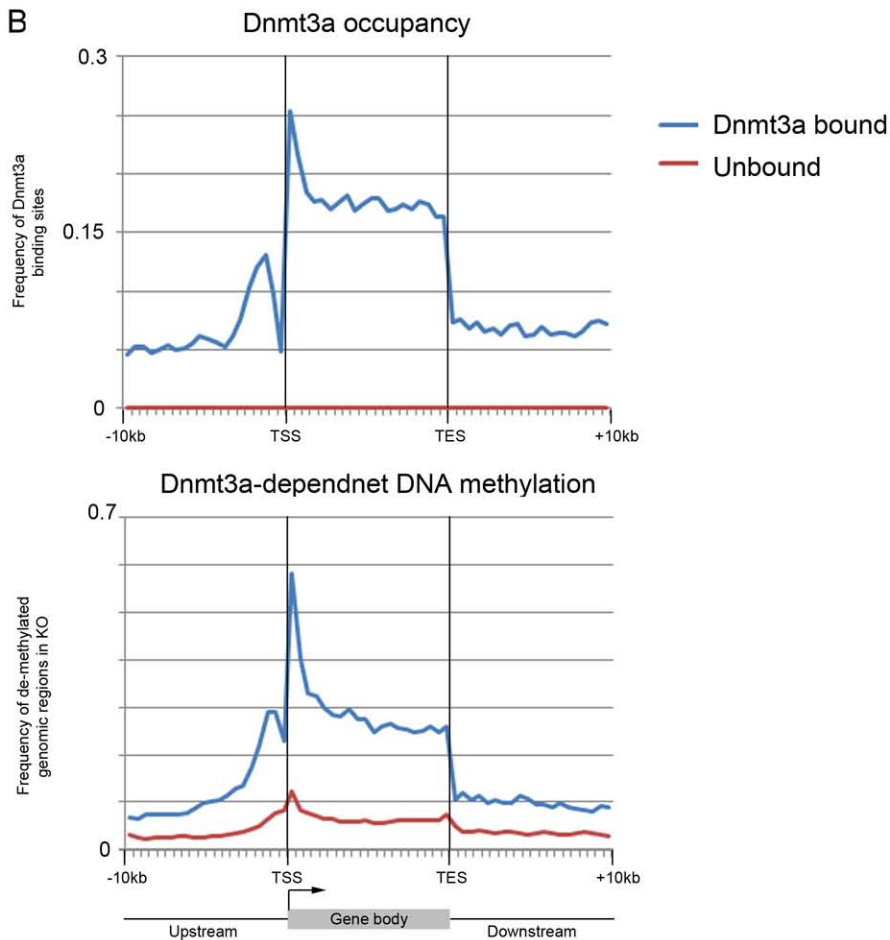
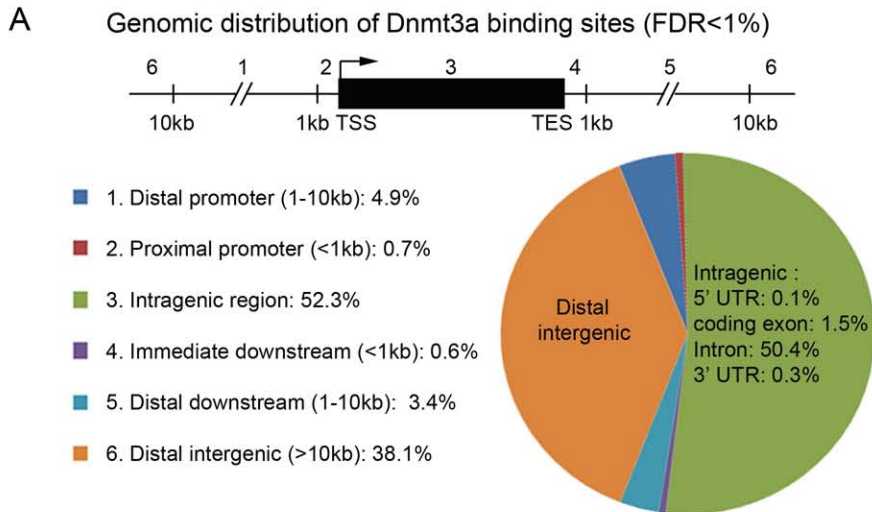


Fig. S9 Genomic analysis of Dnmt3a occupancy and Dnmt3a-dependent DNA methylation in SVZ NSCs. (A) Genomic distribution of Dnmt3a bound sites (FDR<1%) relative to UCSC RefSeq genes (mm8). (B) Averaged peak densities (the percentage of statistically significant peaks) of Dnmt3a (FDR<1%, mapped to 3,271 Refseq genes, mm8) and Dnmt3a-dependent DNA methylation (KS>2) are binned into 500bp windows across genomic regions associated with UCSC Refseq genes (mm8). TSS, transcription start site; TES, transcription end site. The gray bar represents the full-length gene body of all annotated RefSeq genes (n=16,946).

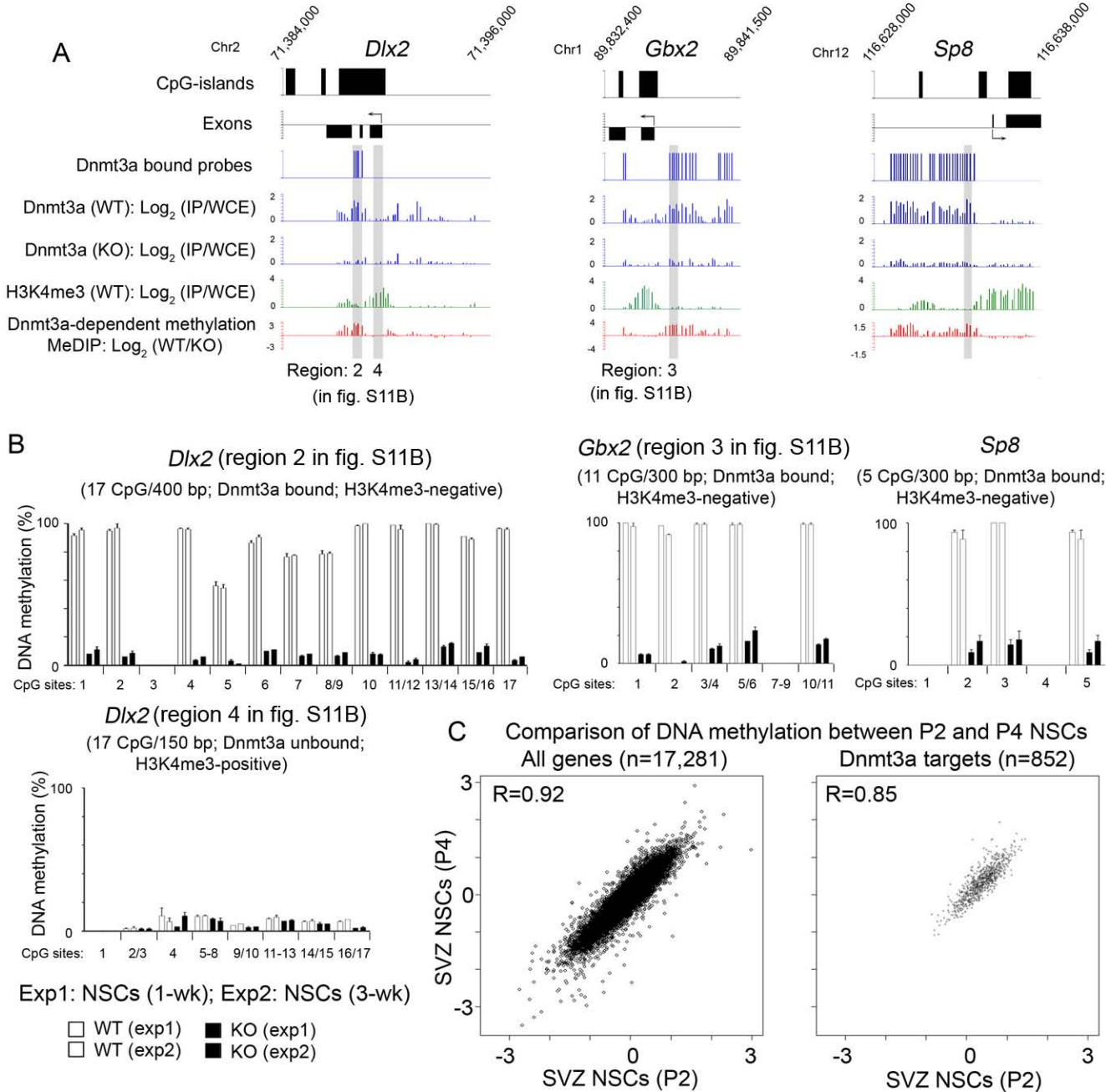


Fig. S10 Limited in vitro culturing does not alter DNA methylation levels on Dnmt3a targets.
 (A) CpG-islands, annotated exons (UCSC Refseq, mm7), Dnmt3a bound probes, and raw enrichment (log₂ ratios) of Dnmt3a, H3K4me3, and DNA methylation in NSCs at passage (P) 4 are shown for three Dnmt3a targets. The Dnmt3a bound regions analyzed by MALDI-TOF MS (shown in B) are shaded in gray.
 (B) Using bisulphite conversion followed by MALDI-TOF MS (Sequenom), DNA methylation levels were determined for three Dnmt3a bound regions (shown in A) with different CpG densities in WT and KO NSCs with short-term (exp1: 1-week/P2) or extended (exp2: 3-week/P4) in vitro culturing. The DNA methylation level of individual CpG site was quantified by averaging two replicate measurements of the same sample. Closely clustered CpG sites are reported as a single value. CpG sites not analyzed are shown as missing in histograms.
 (C) MeDIP-chip analyses of genomic DNA extracted from NSCs at P2 (1-week) or P4 (3-week). The promoter DNA methylation level (MeDIP signal) of each gene was estimated by averaging the log₂ ratio (IP versus total input) of all the probes assigned to the same gene. Scatterplots of promoter DNA methylation between P2 and P4 NSCs are shown for all genes (n=17,281) and for Dnmt3a bound genes (n=852).

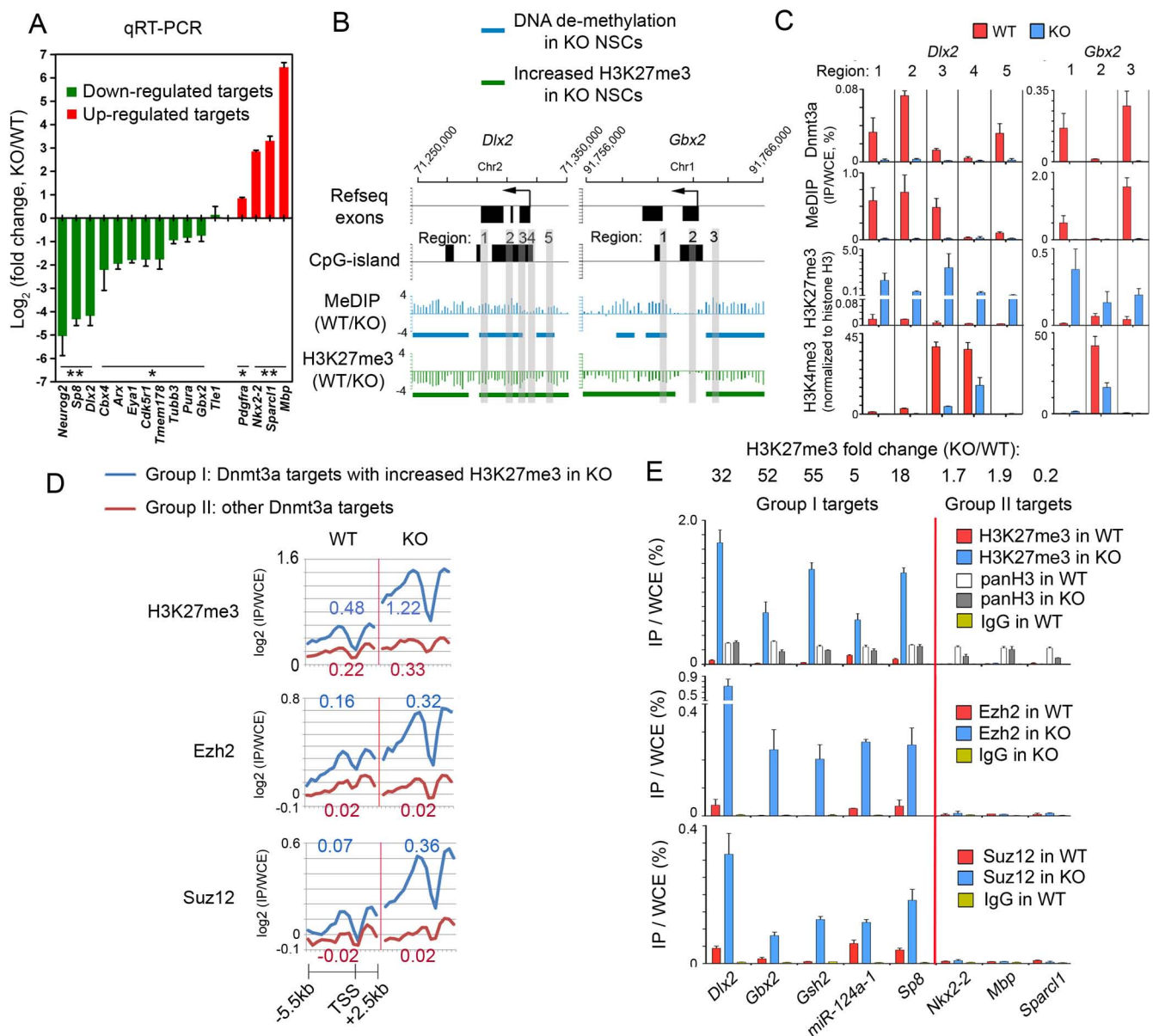


Fig. S11 Dnmt3a antagonizes PRC2/H3K27me3 on Dnmt3a targets down-regulated in KO NSCs.

(A) Quantitative PCR (qPCR) analysis of mRNA levels of 16 Dnmt3a direct targets (identified by expression microarrays as differentially expressed between WT and KO NSCs) in WT and KO NSCs under proliferating conditions. All but one target (Tle1) are confirmed as differentially expressed targets. Error bars represent s.e.m. determined from four independent cultures (*, $P < 0.05$; **, $P < 0.001$; paired two-tailed Student's t-test).

(B) Relative spatial distribution of relative changes in DNA methylation and H3K27me3 within two representative down-regulated Dnmt3a targets in KO NSCs. Regions examined by locus-specific ChIP/MeDIP-qPCR (C) are shaded in gray.

(C) qPCR analysis of Dnmt3a occupancy, DNA methylation, H3K27me3 and H3K4me3 levels within selected loci of Dnmt3a targets in WT and KO NSCs. Error bars, s.e.m. of two experiments.

(D) Distributions of H3K27me3, Ezh2, and Suz12 are shown for these two groups of Dnmt3a targets in WT and KO NSCs. H3K27me3, Ezh2 and Suz12 level increases markedly on a cohort of Dnmt3a targets (Group I: 35.3% of Dnmt3a targets identified by extended promoter microarrays) in *Dnmt3a*-null NSCs.

Mean values of $\log_2 R$ (within -2.5 to $+2.5$ kb) in WT and KO NSCs are also shown for two groups of Dnmt3a targets. Note that the Group I targets are also enriched in the down-regulated Dnmt3a targets in KO NSCs.

(E) ChIP-qPCR analysis of H3K27me3, total histone H3 (panH3), Ezh2 and Suz12 occupancy in WT and KO NSCs for representative Group I or II Dnmt3a targets. Mock ChIP using non-specific rabbit IgG is shown as negative controls. Error bars, s.e.m. of three independent experiments.

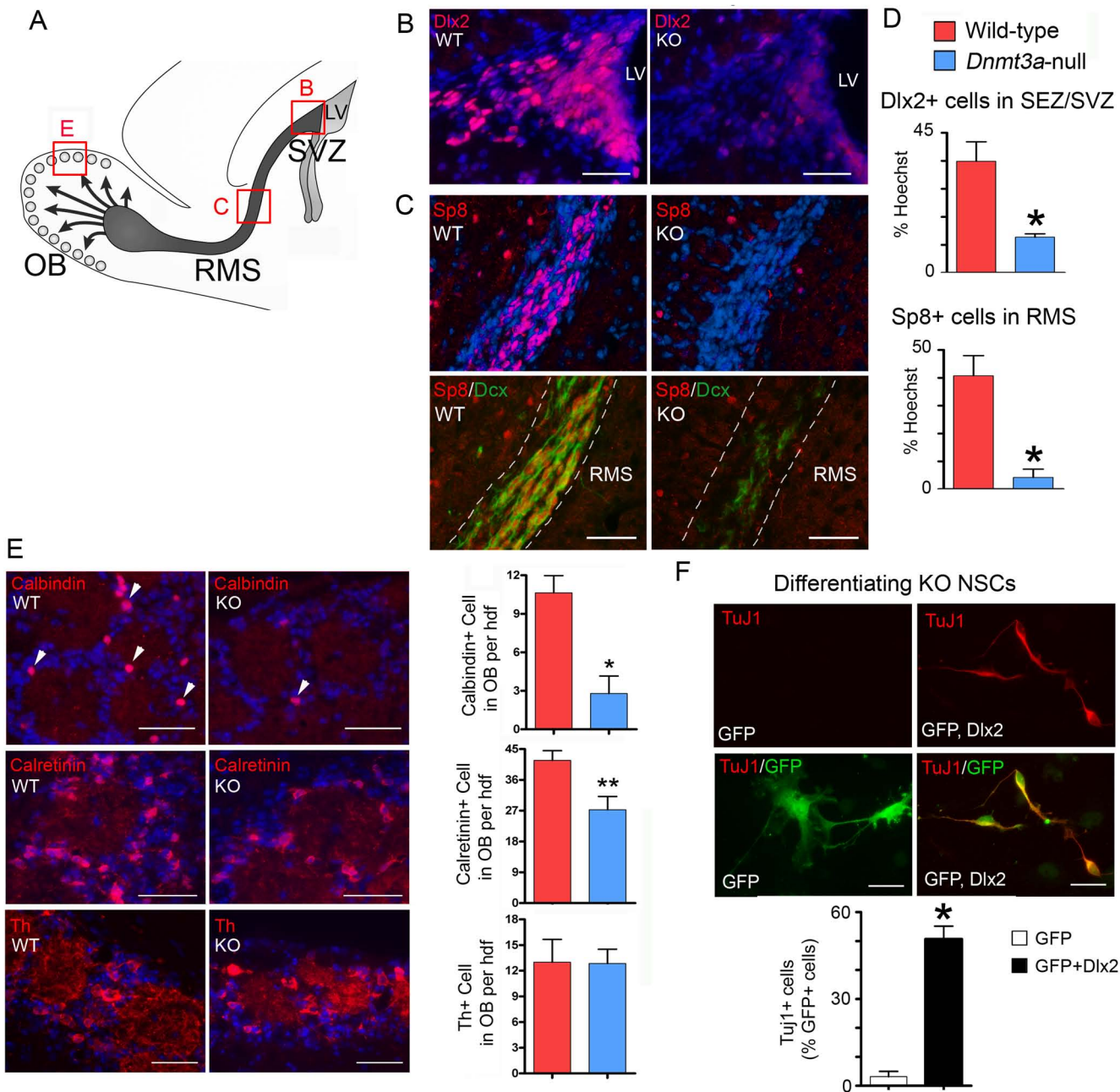


Fig. S12 *Dnmt3a*-deletion impairs expression of neurogenic *Dnmt3a* targets (*Dlx2* and *Sp8*) and generation of *Calbindin*⁺ and *Calretinin*⁺ periglomerular interneurons in OB in vivo. (A) Schematics of olfactory bulb (OB) neurogenesis from postnatal neural stem cells in the SVZ. Red boxes indicate regions shown in (B), (C) and (E). (B-C) Immunohistochemistry for the *Dnmt3a* targets *Dlx2* (B) and *Sp8* (C) in postnatal 3-week sagittal brain sections of WT and KO. Note that *Sp8* was double-labeled with *Dcx*. Scale bars, 50 μ m. (D). Quantification of *Dlx2*⁺ cells in SEZ and *Sp8*⁺ cells in RMS of WT and KO mice at postnatal 3-week. Error bars, s.e.m. (*, $P < 0.05$; $n \geq 3$ animals, paired two-tailed Student's *t*-test). (E) Sample immunofluorescence images of *Calbindin*⁺ (partially *Dlx2*-dependent), *Calretinin*⁺ (partially *Sp8*-dependent) and *Th*⁺ periglomerular neurons in sagittal sections of P24 OB are shown for WT and KO mice. Scale bars, 50 μ m. Quantification of *Calbindin*⁺, *Calretinin*⁺ and *Th*⁺ cells in glomerular layers of WT and KO OB. Error bars, s.e.m. (*, $P = 0.0105$; **, $P < 0.005$, $n = 7$ sections from three pairs of mice). (F) Quantification of *TuJ1*⁺/*GFP*⁺ cells after transfection of GFP alone or both pCAG-*Dlx2* and GFP expression plasmids into *Dnmt3a*-null SEZ NSCs. Transfected KO NSCs were differentiated for 3 days before analysis. Error bars, s.e.m. of triplicate experiments (*, $P < 0.0001$).

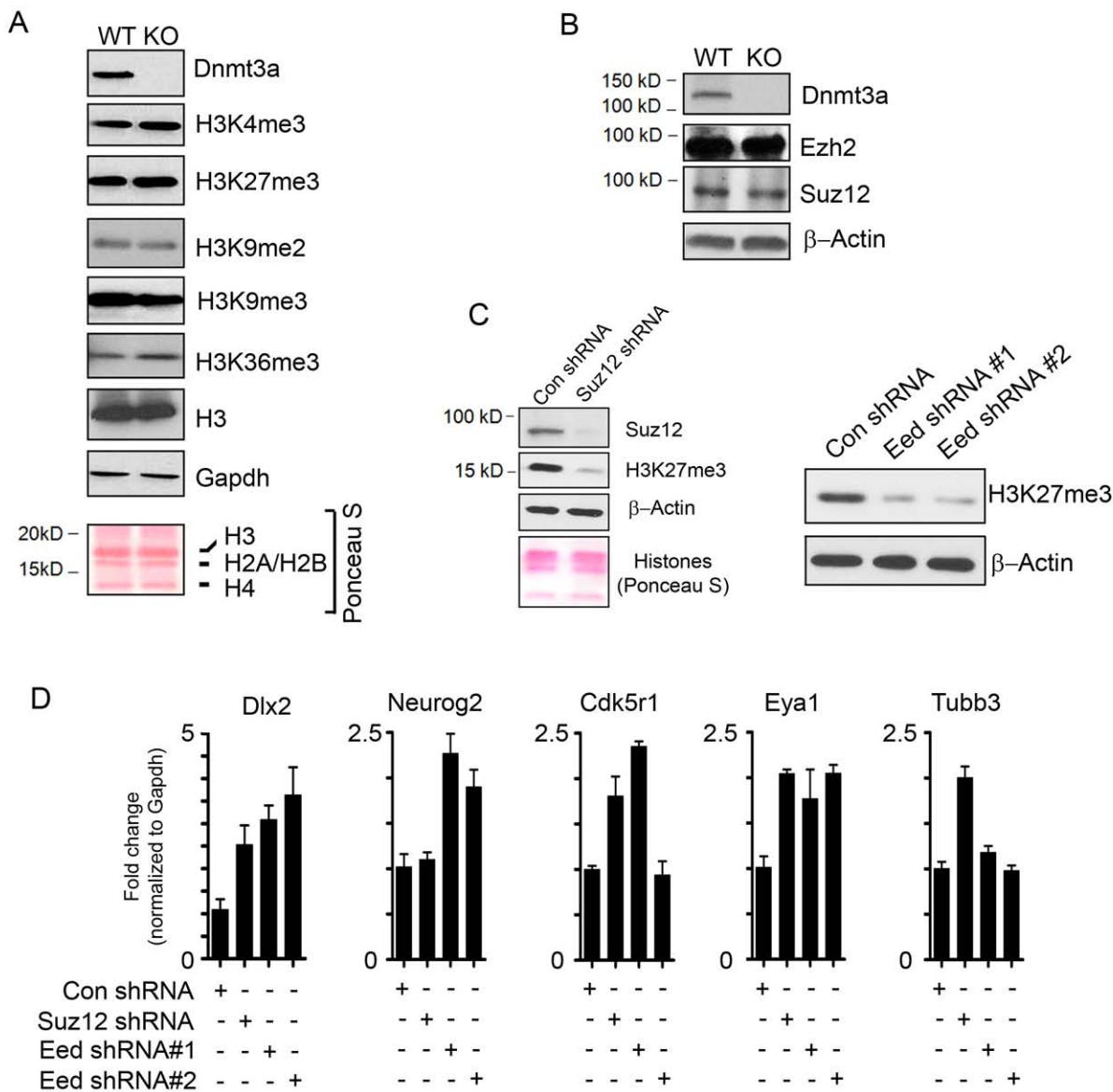


Fig. S13 Inhibiting PRC2 in *Dnmt3a*-null NSCs partially rescue expression of neurogenic *Dnmt3a* targets.

(A) Global levels of histone lysine methylation and PRC2 core subunits are not altered in *Dnmt3a*-null postnatal NSCs. Immunoblotting of site-specific histone lysine methylation in WT and KO NSCs.

Immunoblotting of total histone H3, house-keeping gene *Gapdh* and Ponceau S staining of total histones were used as loading controls.

(B) Immunoblotting of core PRC2 subunits (*Ezh2* and *Suz12*) in WT and KO NSCs.

(C) Immunoblotting of PRC2/H3K27me3 in KO NSCs infected with lentiviruses expressing control shRNAs or shRNAs specific for the core PRC2 subunit *Suz12* or *Eed*.

(D) Quantitative RT-PCR analyses of five neurogenic *Dnmt3a* target in control and PRC2-shRNA infected postnatal *Dnmt3a*-null (KO) NSCs under proliferation conditions.

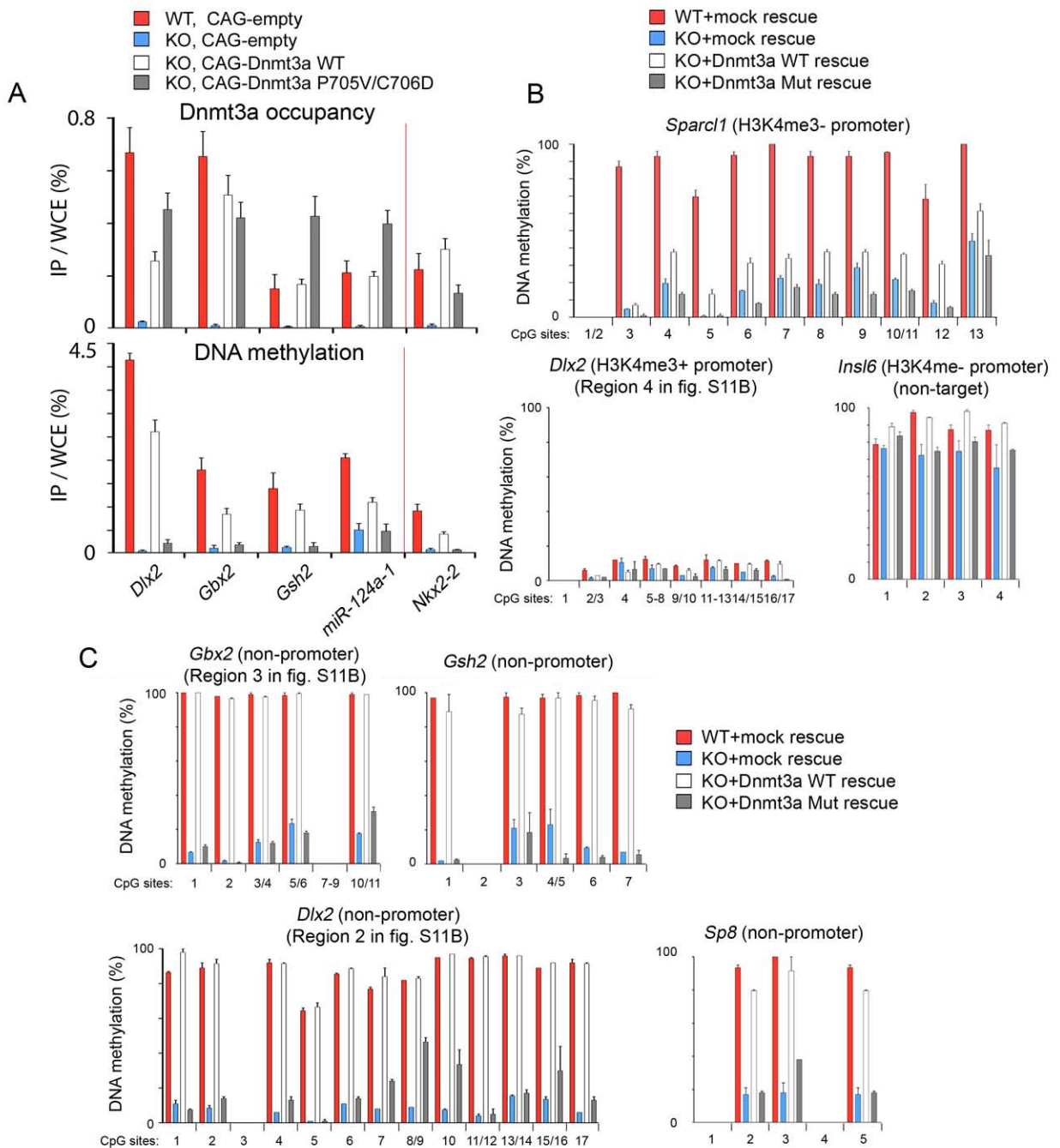


Fig. S14 Characterization of *Dnmt3a*-null NSCs that were rescued with wild-type or catalytically inactive mutant *Dnmt3a*.

(A) Quantitative PCR analysis of *Dnmt3a* and DNA methylation levels in WT, KO, and rescued KO NSCs (transient re-expression of wild-type or catalytically inactive mutant (P705V/C706D) full-length *Dnmt3a*) are shown for six *Dnmt3a* targets. Note that *Nkx2-2* is a *Dnmt3a* target that is not associated with increase in H3K27me3 in KO NSCs.

(B-C) Quantitative DNA methylation analysis by bisulphite Mass Spectrometry (Sequenom MassArray assays) of five *Dnmt3a* bound regions and two unbound regions (*Dlx2*, region 4: a H3K4me3-high promoter region, and *Ins16*: a sperm-specific gene) in rescued NSCs.

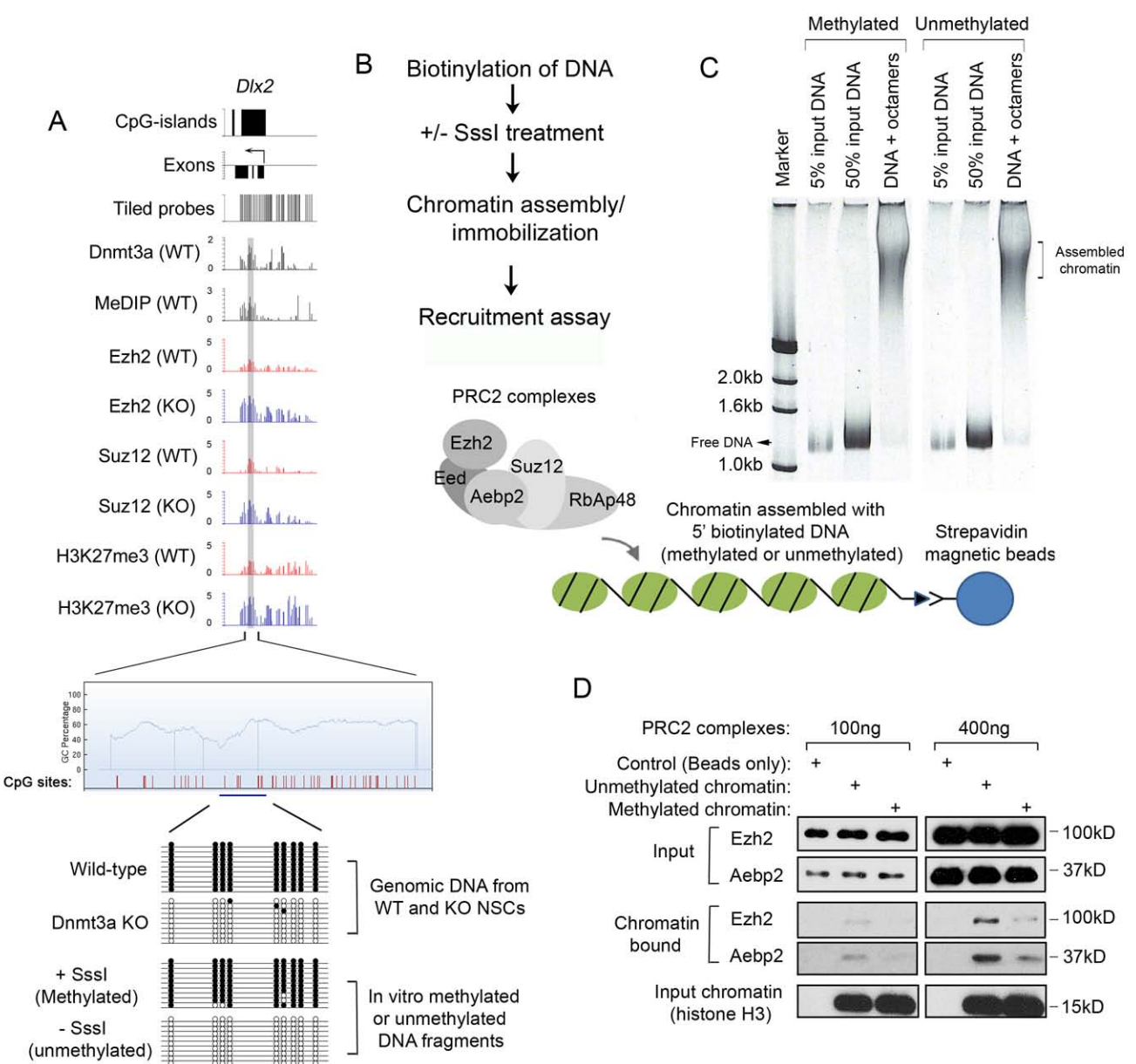


Fig. S15 Recruitment of PRC2 to chromatin is partially inhibited by DNA methylation *in vitro*.

(A) Based on ChIP-chip and MeDIP-chip results, a 1.1 kb genomic region containing Dnmt3a binding sites within the *Dlx2* gene locus was cloned, purified and incubated with or without CpG DNA methylase SssI *in vitro*. CpG sites within the 1.1 kb region were shown as red vertical bars. SssI treatment was confirmed by bisulphite sequencing of a sub-region within the 1.1kb region (blue horizontal bar). As a reference, bisulphite sequencing results of the same region in wild-type and Dnmt3a KO NSCs were shown.

(B) Diagram of experimental design of *in vitro* PRC2 repression complex recruitment assay.

(C) Both methylated and unmethylated DNA (5' biotinylated) can be efficiently assembled into chromatin arrays (shifted smear) using recombinant *Xenopus* octamers.

(D) Western blotting of bound fraction of PRC2 subunits on methylated or unmethylated chromatin arrays. Equal amount of PRC2 complexes (100ng or 400ng) was incubated with only beads (without chromatin), and beads with immobilized unmethylated or methylated chromatin (100ng). After 30 min incubation, the beads were stringently washed and resuspended in the SDS sampling buffer for SDS-PAGE. The chromatin bound fraction of PRC2 complexes was detected by immunoblotting of Aebp2 (Flag-tagged) and Ezh2. The relative binding was quantified by densitometry (in Fig. 4C).

Histone modification levels

 ● Methylated CpGs
 ○ Unmethylated CpGs

Dnmt3a-dependent non-promoter DNA methylation promotes transcription of CpG-rich, H3K4me3-high targets

Dnmt3a-dependent promoter DNA methylation represses transcription of CpG-poor, H3K4me3-low targets

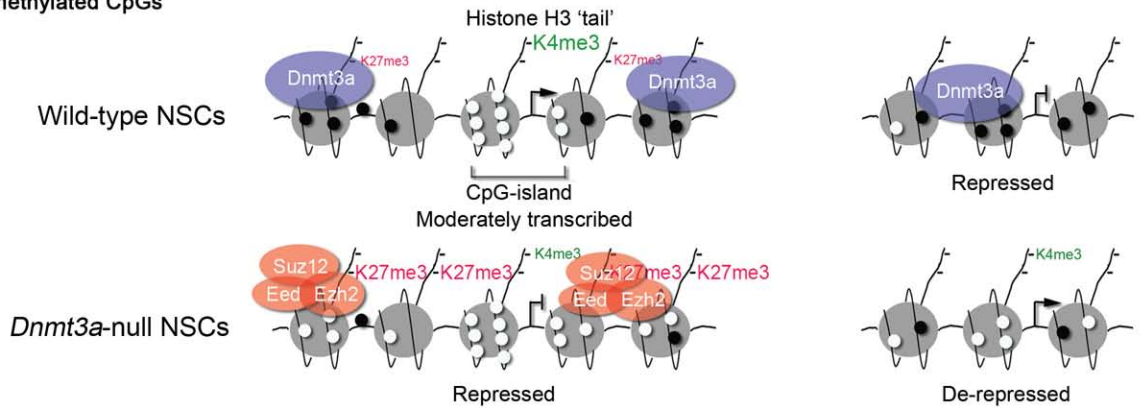


Fig. S16 A A proposed model of Dnmt3a-dependent non-proximal promoter DNA methylation in antagonizing Polycomb repression and promoting transcription in postnatal neural stem cells.

In multipotent postnatal NSCs, antagonism between Dnmt3a-mediated DNA methylation and PRC2-mediated repressive histone modification H3K27me3 primarily takes place on Dnmt3a targets with CpG-island containing gene promoters, many of which encode regulators of neurogenesis. The font size of 'H3K4me3' (green) or 'H3K27me3' (red) represents relative levels of indicated histone modifications. Black circles represent methylated CpG dinucleotides, whereas white circles represent unmethylated CpG dinucleotides.

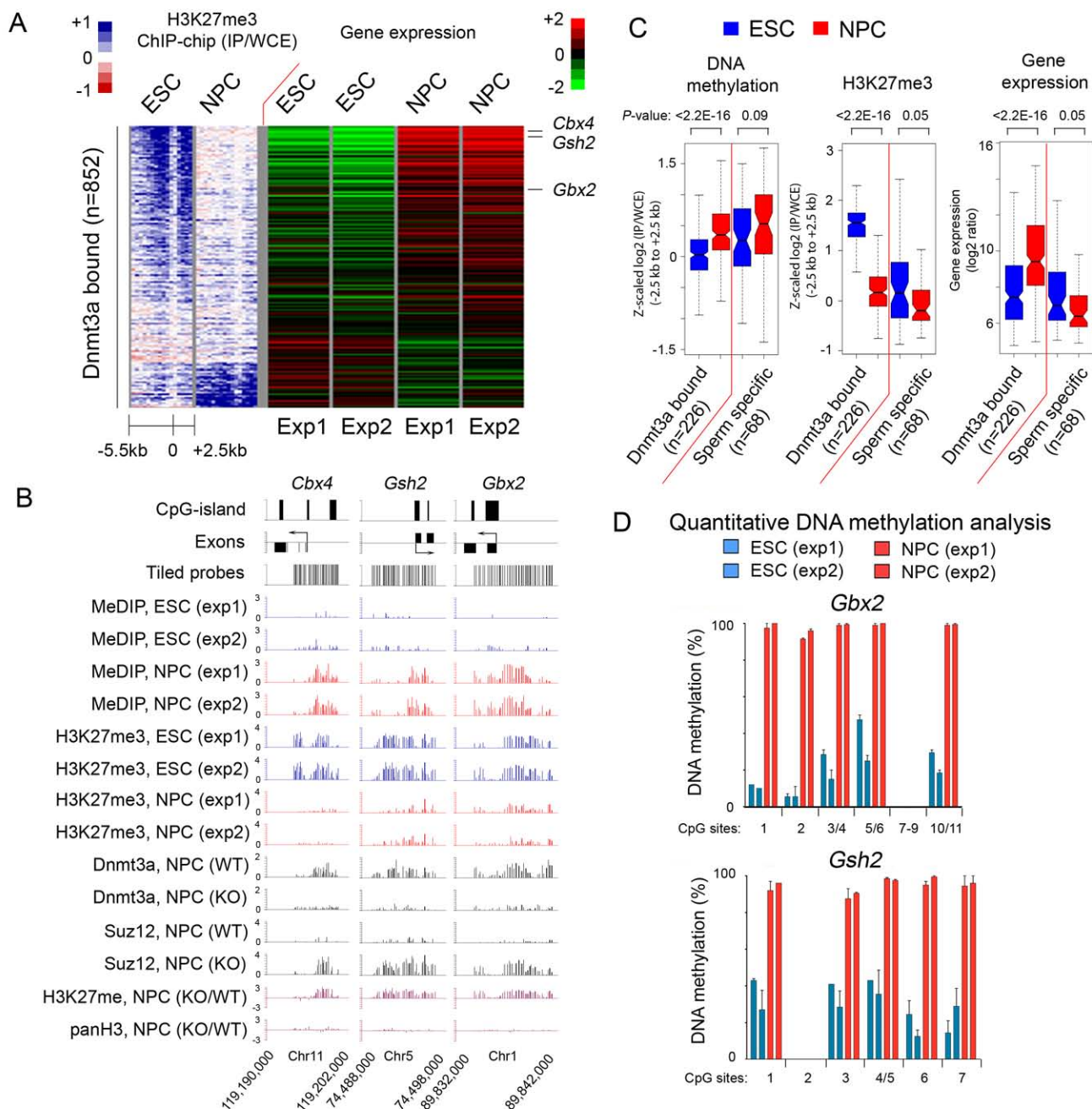


Fig. S17 Reduction in H3K27me3 levels on many genes (PcG targets in ESCs, Dnmt3a targets in NPCs) during the conversion of ESCs to NPCs is accompanied by *de novo* DNA methylation and a concomitant increase in basal transcriptional levels.

(A) Composite heatmaps of H3K27me3 and gene expression profiling in ESCs and NPCs are shown for Dnmt3a targets in NPCs (n=852). Genes were ranked by the difference (Z-scaled \log_2 ratios) in H3K27me3 between ESCs and NPCs.

(B) Raw enrichment of DNA methylation and H3K27me3 in ESCs and NPCs with indicated genotypes are shown for three Dnmt3a targets in NPCs.

(C) Reduction in H3K27me3 on many Dnmt3a targets (in NPCs) during ESC differentiation is accompanied by *de novo* DNA methylation and a concomitant increase in basal transcriptional levels. Boxplots of the normalized levels of DNA methylation, H3K27me3, and gene expression in ESCs and NPCs are shown for Dnmt3a targets associated with a significant loss of H3K27me3 from ESCs to NPCs (n=226). A group of sperm-specific genes is also shown as positive controls for DNA methylation (n=68).

(D) Sequenom MassArray DNA methylation analyses of two Dnmt3a targets during ESC to NPC conversion.

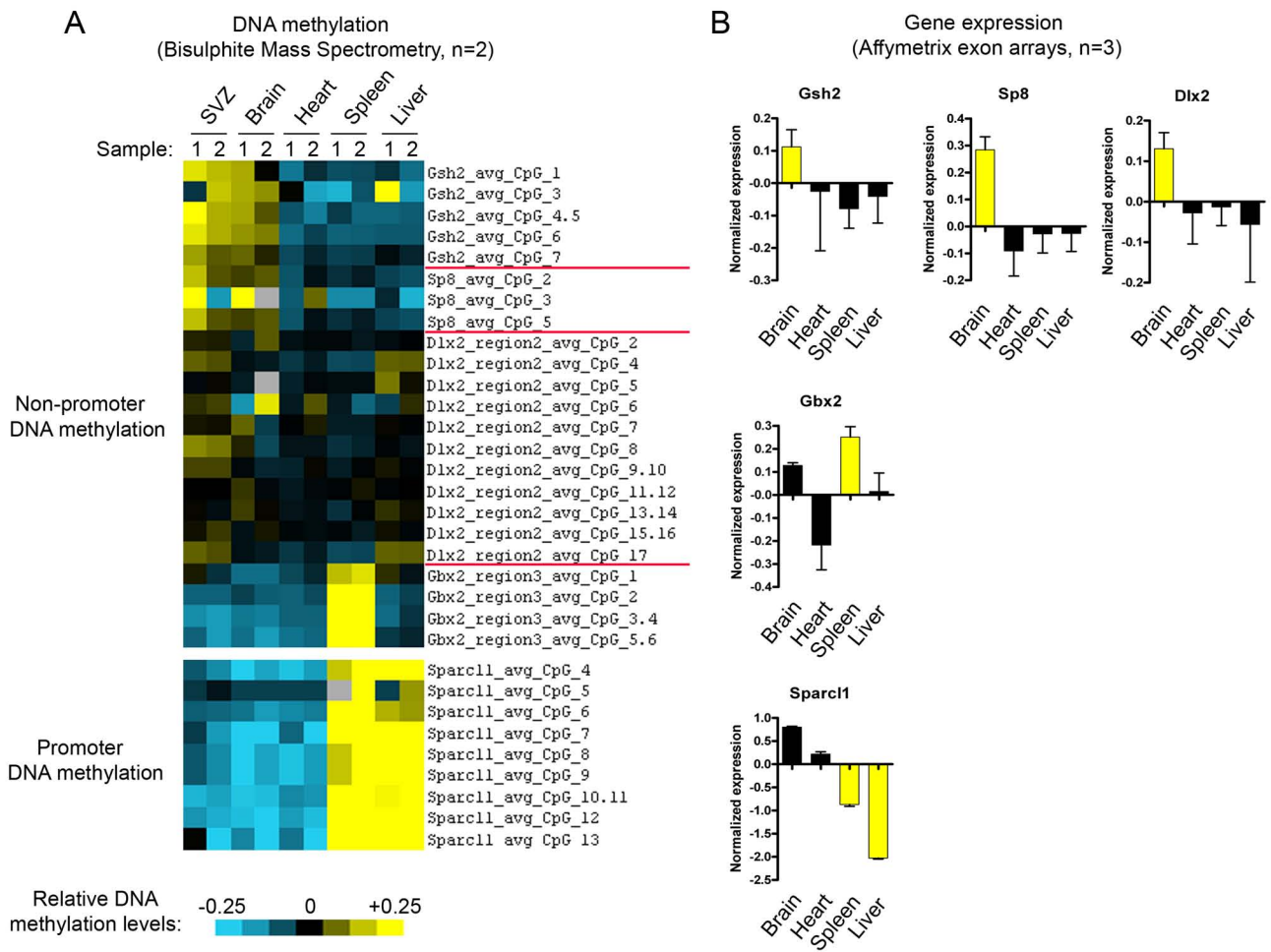


Fig. S18 Non-promoter DNA methylation positively correlates with tissue-specific transcription in vivo.

(A) Heatmap representation of quantitative DNA methylation analysis by Sequenom MassArray analyses of five Dnmt3a bound regions (amplicons in fig. S14B-C; 4 non-promoter: *Dlx2*, *Gsh2*, *Sp8* and *Gbx2*; one promoter: *Sparcl1*) in five postnatal tissues (SVZ at postnatal day (P) 18; brain, heart, spleen and liver at P45). The relative methylation levels were represented by color intensity (mean-centered values). Yellow color represents higher methylation levels, whereas blue represents lower methylation levels. Missing values are in gray. Each row represents a CpG unit (single or closely clustered CpG sites) measured by Sequenom bisulphite Mass Spectrometry assays. Each column represents a tissue sample. Two biological independent samples (one male and one female wild-type littermates) were measured in duplicate for each tissue. While promoter DNA methylation at *Sparcl1* is negatively correlated with gene expression, non-promoter DNA methylation at other genes is generally associated with higher levels tissue-specific transcription.

(B) Relative gene expression data (in triplicates) in adult mouse brain, heart, spleen and liver are retrieved from a published database via UCSC Table browser (A. Pohl, *et al.*, *Bioinformatics* **25**, 2442 (2009)). The gene expression was measured by Affymetrix Mouse Exon 1.0 ST arrays. The quantile normalized data were further converted to median-centered log-ratios. The expression of each target was estimated by averaging the expression values of all anti-sense exon probes covered by the gene body. The tissues associated with relatively high level of DNA methylation are highlighted in yellow.

Table S1 Gene ontology (GO) analysis of differentially expressed genes between differentiating WT and KO SEZ cells (DAVID <http://david.abcc.ncifcrf.gov>)

Note: P-value were corrected for multiple testing and the cutoff for significantly enriched GO term was P-value<0.01. The total number of genes included in GO analysis is 14,977.

Down-regulated genes in differentiating KO SEZ cells

<u>GO Term</u>	<u>% Total</u>	<u>Enrichment</u>	<u>Corrected P-value</u>
GO:0007399~nervous system development	8.64%	2.58	1.34E-15
GO:0007275~multicellular organismal development	18.19%	1.61	1.85E-10
GO:0030182~neuron differentiation	4.65%	3.08	1.80E-10
GO:0048666~neuron development	3.99%	3.34	4.46E-10
GO:0032502~developmental process	22.26%	1.48	1.16E-09
GO:0022008~neurogenesis	4.98%	2.69	4.38E-09
GO:0048699~generation of neurons	4.73%	2.76	4.63E-09
GO:0048731~system development	14.12%	1.62	4.26E-08
GO:0030154~cell differentiation	14.70%	1.60	4.35E-08
GO:0048869~cellular developmental process	14.70%	1.60	4.35E-08
GO:0031175~neurite development	3.41%	3.22	3.69E-08
GO:0048856~anatomical structure development	15.95%	1.56	3.90E-08
GO:0065007~biological regulation	29.73%	1.30	5.67E-07
GO:0030030~cell projection organization and biogenesis	3.90%	2.65	7.68E-07
GO:0048858~cell projection morphogenesis	3.90%	2.65	7.68E-07
GO:0032990~cell part morphogenesis	3.90%	2.65	7.68E-07
GO:0050789~regulation of biological process	27.41%	1.31	1.10E-06
GO:0007409~axonogenesis	2.74%	3.24	1.67E-06
GO:0007156~homophilic cell adhesion	2.24%	3.73	2.45E-06
GO:0048667~neuron morphogenesis during differentiation	2.74%	3.05	7.26E-06
GO:0048812~neurite morphogenesis	2.74%	3.05	7.26E-06
GO:0016337~cell-cell adhesion	3.41%	2.61	1.04E-05
GO:0007268~synaptic transmission	2.91%	2.77	2.49E-05
GO:0019226~transmission of nerve impulse	3.24%	2.57	3.21E-05
GO:0000904~cellular morphogenesis during differentiation	2.82%	2.79	3.20E-05
GO:0050794~regulation of cellular process	24.42%	1.29	6.35E-05
GO:0007267~cell-cell signaling	4.07%	2.20	7.08E-05
GO:0048519~negative regulation of biological process	8.31%	1.62	2.33E-04
GO:0048523~negative regulation of cellular process	7.89%	1.65	2.28E-04
GO:0019222~regulation of metabolic process	17.77%	1.34	3.37E-04
GO:0048468~cell development	9.39%	1.53	6.65E-04
GO:0031323~regulation of cellular metabolic process	17.03%	1.33	8.31E-04
GO:0032989~cellular structure morphogenesis	4.90%	1.86	9.27E-04
GO:0000902~cell morphogenesis	4.90%	1.86	9.27E-04
GO:0009653~anatomical structure morphogenesis	9.05%	1.53	9.32E-04
GO:0010468~regulation of gene expression	16.45%	1.34	9.93E-04
GO:0016126~sterol biosynthetic process	0.91%	5.93	0.001085264
GO:0022610~biological adhesion	5.81%	1.72	0.001249485
GO:0007155~cell adhesion	5.81%	1.72	0.001249485
GO:0003001~generation of a signal involved in cell-cell signaling	1.58%	3.18	0.003020177
GO:0045449~regulation of transcription	15.28%	1.33	0.003401544

GO:0009892~negative regulation of metabolic process	3.82%	1.93	0.003472134
GO:0006355~regulation of transcription, DNA-dependent	14.62%	1.33	0.003775592
GO:0048489~synaptic vesicle transport	0.83%	5.76	0.003713862
GO:0032501~multicellular organismal process	25.08%	1.22	0.003954148
GO:0007269~neurotransmitter secretion	1.16%	3.97	0.00397036
GO:0006351~transcription, DNA-dependent	14.70%	1.33	0.004286769
GO:0032774~RNA biosynthetic process	14.70%	1.32	0.004838642
GO:0001505~regulation of neurotransmitter levels	1.50%	3.10	0.005750093
GO:0007411~axon guidance	1.41%	3.23	0.005848214

Up-regulated genes in differentiating KO SEZ cells

<u>GO Term</u>	<u>% Total</u>	<u>Enrichment</u>	<u>Corrected P-value</u>
GO:0007049~cell cycle	7.99%	2.17	7.53E-15
GO:0048856~anatomical structure development	16.70%	1.63	8.25E-15
GO:0048731~system development	14.55%	1.67	4.10E-14
GO:0032502~developmental process	22.06%	1.47	1.44E-13
GO:0022402~cell cycle process	6.62%	2.23	6.92E-13
GO:0007275~multicellular organismal development	17.29%	1.53	3.65E-12
GO:0022403~cell cycle phase	4.17%	2.74	8.15E-12
GO:0000279~M phase	3.70%	2.90	1.85E-11
GO:0048513~organ development	11.69%	1.66	1.67E-10
GO:0051301~cell division	3.34%	2.73	3.88E-09
GO:0000278~mitotic cell cycle	3.46%	2.67	4.14E-09
GO:0007067~mitosis	2.86%	3.00	4.18E-09
GO:0000087~M phase of mitotic cell cycle	2.86%	2.98	4.70E-09
GO:0009653~anatomical structure morphogenesis	9.78%	1.65	2.21E-08
GO:0006950~response to stress	7.10%	1.70	2.47E-06
GO:0000074~regulation of progression through cell cycle	3.88%	2.10	4.95E-06
GO:0051726~regulation of cell cycle	3.88%	2.08	6.41E-06
GO:0048869~cellular developmental process	13.00%	1.42	9.82E-06
GO:0030154~cell differentiation	13.00%	1.42	9.82E-06
GO:0009887~organ morphogenesis	4.83%	1.84	2.50E-05
GO:0065007~biological regulation	27.79%	1.21	3.98E-05
GO:0048514~blood vessel morphogenesis	2.39%	2.47	4.06E-05
GO:0048468~cell development	9.06%	1.48	1.02E-04
GO:0048522~positive regulation of cellular process	7.04%	1.58	1.03E-04
GO:0001568~blood vessel development	2.56%	2.29	1.04E-04
GO:0048518~positive regulation of biological process	7.81%	1.53	1.06E-04
GO:0001525~angiogenesis	1.97%	2.60	1.39E-04
GO:0001944~vasculature development	2.56%	2.26	1.40E-04
GO:0050789~regulation of biological process	25.34%	1.21	1.82E-04
GO:0048646~anatomical structure formation	2.33%	2.28	3.58E-04
GO:0022008~neurogenesis	3.52%	1.90	3.96E-04
GO:0008283~cell proliferation	4.53%	1.69	9.30E-04
GO:0009966~regulation of signal transduction	3.94%	1.76	0.001108842
GO:0007399~nervous system development	5.37%	1.60	0.001129143
GO:0006629~lipid metabolic process	5.25%	1.61	0.001168061
GO:0048699~generation of neurons	3.22%	1.88	0.001301783
GO:0032787~monocarboxylic acid metabolic process	2.33%	2.05	0.003762921
GO:0007010~cytoskeleton organization and biogenesis	4.35%	1.63	0.004565965

GO:0007059~chromosome segregation	0.95%	3.31	0.007267371
GO:0001501~skeletal development	1.97%	2.12	0.008465342
GO:0048519~negative regulation of biological process	7.22%	1.41	0.008892936
GO:0009611~response to wounding	2.86%	1.81	0.008990888
GO:0050793~regulation of developmental process	2.74%	1.84	0.009077248
GO:0006468~protein amino acid phosphorylation	5.01%	1.53	0.009810011

Table S2 Primer sequences

ChIP/MeDIP-qPCR primers

<i>2700055K07Rik_ChIP_F</i>	CTGTCCAGAGACCTTTCCTAACCC
<i>2700055K07Rik_ChIP_R</i>	TACCCAAGACTCAGCAATATCCGC
<i>Cdk5r1_ChIP_F</i>	GTGTCAGCGAAGAAGAAGAACTCC
<i>Cdk5r1_ChIP_R</i>	TCATTGTTGAGATGCGCGATGTTG
<i>Chl1_ChIP_F</i>	ACCAGACAGATCGGATGTCAAGAG
<i>Chl1_ChIP_R</i>	TTTCCTTCCACCTCCCTCAAAGAG
<i>Cpxm2_ChIP_F</i>	TGCACCAGTATTCTATGGCTCCTC
<i>Cpxm2_ChIP_R</i>	TCTCACCACAAATGAGTCCCTCAG
<i>Dlx2 (region 1)_ChIP_F</i>	AAACATAGGGACTGCTGAGGTC
<i>Dlx2 (region 1)_ChIP_R</i>	GCAGAGTTTGTAATAAGGGTGTG
<i>Dlx2 (region 2)_ChIP_F</i>	ATGTGACCAAGGTTCTGGGTAGTG
<i>Dlx2 (region 2)_ChIP_R</i>	CATGGGAGGAAAGAAAATGACCCG
<i>Dlx2 (region 3)_ChIP_F</i>	CGGAGTAGGAGACATTGTTGAG
<i>Dlx2 (region 3)_ChIP_R</i>	TACTACACCAACCAGCAGCAC
<i>Dlx2 (region 4)_ChIP_F</i>	GAGCAGCTTTACGATTGTCTG
<i>Dlx2 (region 4)_ChIP_R</i>	ATTCCTTCTGATTGGCTGTTG
<i>Dlx2 (region 5)_ChIP_F</i>	GACAGTGTAGGAGTTGTTACAGG
<i>Dlx2 (region 5)_ChIP_R</i>	GTTATGTCTTTAGGAAGGGATGC
<i>Dkk3_ChIP_F</i>	GGAAATCAACCTATTCCAGCAGGC
<i>Dkk3_ChIP_R</i>	CAAGTGGGTTGGGTGTTTACCATC
<i>Foxp2_ChIP_F</i>	TCTGGAGGCACTAAAACAGGAGAC
<i>Foxp2_ChIP_R</i>	AACTTGCTGGAGACAAAACAGCAG
<i>Gbx2 (region 1)_ChIP_F</i>	CCAGCAGATTGTCTTTCTACCAC
<i>Gbx2 (region 1)_ChIP_R</i>	TCTACTGTCTCCTCCTCCTTTG
<i>Gbx2 (region 2)_ChIP_F</i>	TCTATGCTGAAGGCGGTACTACTC
<i>Gbx2 (region 2)_ChIP_R</i>	TCGTCTCTCCCTGGCTTCTC
<i>Gbx2 (region 3)_ChIP_F</i>	GGGGTTAGGAGATTGGAGGGATTG
<i>Gbx2 (region 3)_ChIP_R</i>	CAAGGAATCTGAAGAACAGGCAGG
<i>Gfap_ChIP_F</i>	AGATTTAGTCCAACCCGTTCTC
<i>Gfap_ChIP_R</i>	GGAGTCATTGAGACAAGGAGAAG
<i>Gsh2_ChIP_F</i>	CTGGAGTGCTTGGTTTCTAAGCTG
<i>Gsh2_ChIP_R</i>	CACCACATTCATATCTGCCCTTGC
<i>Id4_ChIP_F</i>	TCAGTGAAAATGAAGGCAGCAGTC
<i>Id4_ChIP_R</i>	AAACAACCAAGCTCTTCAGATGGC
<i>Ins16_ChIP_F</i>	TTATTTGCATGCCTAATTTTGAGTG
<i>Ins16_ChIP_R</i>	CCTTTGTAGGAAAATGGATACAAGTG
<i>Mbp_ChIP_F</i>	GGAAATGCTTTGGCTTGATTGCTG
<i>Mbp_ChIP_R</i>	CTAACCTGGATTGAGCTTGCTTGG
<i>miR-124a-1_ChIP_F</i>	TATGAAAGTGGTCAGTGCTCCAG
<i>miR-124a-1_ChIP_R</i>	ATTGAGAATCTTAGGAGGGGTGGG
<i>Nes_ChIP_F</i>	TATGAATACCCTCGCTTCAGCTCG

Nes_ChIP_R
Neurog1_ChIP_F
Neurog1_ChIP_R
Nkx2-2_ChIP_F
Nkx2-2_ChIP_R
Nkx6-2_ChIP_F
Nkx6-2_ChIP_R
Olig1_ChIP_F
Olig1_ChIP_R
Olig2_ChIP_F
Olig2_ChIP_R
Pdgfra_ChIP_F
Pdgfra_ChIP_R
Slc6a6_ChIP_F
Slc6a6_ChIP_R
Sp8_ChIP_F
Sp8_ChIP_R
Sparcl1_ChIP_F
Sparcl1_ChIP_R

CGGACGTGGAGCACTAGAGAAG
GCCGTACTTAAGGGGTCCTG
AGGGGCTCAGGGAGTGAAT
GGACTTCTTTGAGGATCAGGGGAG
AAGGAAATGGACAGGGTCTAGGTG
GAAATCCTTGAAGTTGGGTTGGGG
TTGCCAGAAAGCAATAAGCAGGAG
AGCAAGTGTGTTTCATAGCAAACGG
CAGAACAGCAGATGTGGGTCCTC
GGGTTTCATTGAGCGGAATTAG
CTCGGTCTGTAATAAGCATCCAC
TAAGTGGCTCCGAAGGGATAAAGG
TTTTGAAAGGCTGGATTGTGAGGC
TAGGACAATGGATTCAGGCTGGTC
TGCTTGCCCACCTTCTTTTCTTTT
GCTTGCTCAAACCATAGATGCTCC
TTTTCTCAGGTAACCCCACTGTGC
GTGTAAGCATTGGCTCTTCATGC
TGATCCTTCTGTCCTTTCACCCTG

RT-qPCR primers

Arx_RT_F
Arx_RT_R
Cbx4_RT_F
Cbx4_RT_R
Cdk5r1_RT_F
Cdk5r1_RT_R
Dlx2_RT_F
Dlx2_RT_R
Eya1_RT_F
Eya1_RT_R
Gapdh_RT_F
Gapdh_RT_R
Gbx2_RT_F
Gbx2_RT_R
Gfap_RT_F
Gfap_RT_R
Mbp_RT_F
Mbp_RT_R
Neurog2_RT_F
Neurog2_RT_R
Nkx2-2_RT_F
Nkx2-2_RT_R

ATCACCTGCGCTTGATTCCGGCCTG
AAGAGCCTGCCAAATGCTGGGCTG
AAAGCCGAAGTGCCCTGCAAACGC
TCTGGCTTGGTGGTGAGCTGTAGCG
CCCTTCCTGGTAGAGAGCTG
GTGAAATAGTGTGGGTCGGC
CAAAGCAGCTACGACCTGG
CGGACTTTCTTTGGCTTCCC
AACACGTGGGAGGTCTGCTTGGC
TTGCCAATGCTGGGATGAGCTGCG
CTGAGTTCGTGGAGTCTACTGG
GTCATATTTCTCGTGGTTCACACC
CAAACCTCAGCGAGGTGCAAG
AATCTTGGGGTTCCGAGAGG
CAGGAGTACCACGATCTACTCAAC
GGAGAAAGTCTGTACAGGAATGGT
ACAGAAGAGACCCTCACAGC
CTGTCACCGCTAAAGAAGCG
TCAAGAAGACCCGCAGGCTCAAGGC
GATGTAATTGTGGGCGAAGCGCAGC
GACACCAACGATGAAGACGG
TGCTGTCGTAGAAAGGGCTC

<i>Pura_RT_F</i>	TGGGCCAAGTTCGGACACACCTTC
<i>Pura_RT_R</i>	TTGCTGCTGCTGTTGCTGCTGGTG
<i>Sp8_RT_F</i>	ATAGCTCCCATCAGCCAGTG
<i>Sp8_RT_R</i>	AACCAGGACTCATACGGGTG
<i>Sparcl1_RT_F</i>	TGCAAAACCGATCCACAAGG
<i>Sparcl1_RT_R</i>	CTGGCGTAGGTTTGTTGTC
<i>Teme178_RT_F</i>	TCACGGCCATCTTCACCGACCACTG
<i>Teme178_RT_R</i>	ACAGCGGCATCAGGCGGTTCTTCTG
<i>Tle1_RT_F</i>	AATTCCAGGGCCACACAGACGGAGC
<i>Tle1_RT_R</i>	TTCCATGCCACAGCAAGCCACTC
<i>Tubb3_RT_F</i>	ATACTACAATGAGGCCTCCTCTCAC
<i>Tubb3_RT_R</i>	GCACCACTCTGACCAAAGATAAAG

Bisulphite sequencing primers

<i>Dlx2 (region 1)_BS-Seq_F</i>	TTTTGTATTTTAAGAATAAAGATTTTAGGATAAG
<i>Dlx2 (region 1)_BS-Seq_R</i>	ATAAAAATATCTATACAAATTTCCCCACAT
<i>Dlx2 (region 2)_BS-Seq_F</i>	TAAGTATTGGGTTTAGAAGTTTATTTTGT
<i>Dlx2 (region 2)_BS-Seq_R</i>	ACCATCTACTCCAATTTCCAATAAC
<i>Dlx2 (region 3)_BS-Seq_F</i>	GGATTGTTTTTATTTTATGTTTATT
<i>Dlx2 (region 3)_BS-Seq_R</i>	ACAACACTACACCAACCAACAACA
<i>Dlx2 (region 4a)_BS-Seq_F</i>	TGTTGTTGGTTGGTGTAGTAGTTGT
<i>Dlx2 (region 4a)_BS-Seq_R</i>	TAATTACATTAATTACTAAAAAAACCC
<i>Dlx2 (region 4b)_BS-Seq_F</i>	TTTAGTAATAGTTAATTAGAAGGAATGAGT
<i>Dlx2 (region 4b)_BS-Seq_R</i>	CCCCTTTCTACAATACTTATACAC
<i>Dlx2 (region 5)_BS-Seq_F</i>	TTTTTTTTAAGTGATGAGTTTTTTTT
<i>Dlx2 (region 5)_BS-Seq_R</i>	TTTTAAAATATCAACTTATTTTCCATTAAC
<i>Gbx2 (region 1)_BS-Seq_F</i>	TTTTTTTTATTTGGGTATTTTATTTTTATTTT
<i>Gbx2 (region 1)_BS-Seq_R</i>	AAAAAAATATTCTCTTAAACCTCAAATCC
<i>Gbx2 (region 2)_BS-Seq_F</i>	GAGTGGTTATGAGCGTGGAGGTGAG
<i>Gbx2 (region 2)_BS-Seq_R</i>	GCTAAAAATAATACCGCCTTCAACATAAAC
<i>Gbx2 (region 3)_BS-Seq_F</i>	TTGAGTTTTTTAAGATATTTTTTTTGT
<i>Gbx2 (region 3)_BS-Seq_R</i>	ACTCCTTAACCTAATACTATCAACAATTCC
<i>Gfap_BS-Seq_F</i>	TGTAGGTAAGTAATTTATGGATTAA
<i>Gfap_BS-Seq_R</i>	AAAAAAAATCCACCCTAACAAAAA
<i>Nkx2-2_BS-Seq_F</i>	GGGTTATTGTTTTAGTAATGGAGGTAGTTATAGT
<i>Nkx2-2_BS-Seq_R</i>	ATTTTCAATCAAAAACATCTTAAACCTTCC
<i>Sparcl1_BS-Seq_F</i>	ATTGATTGGGTTGGGTAAGAGTAGGTTAT
<i>Sparcl1_BS-Seq_R</i>	AAACTTCACACTCTTATTTATTCCTAAAAC
<i>Pdgfra_BS-Seq_F</i>	GTTTGGTTTTTTGGTAGTGGGTTA
<i>Pdgfra_BS-Seq_R</i>	TCCACACACACACTTCTCCTAATA

Sequenom BS-MS analysis primers

Dlx2 (region 2)_BS-MS_F

<i>Dlx2 (region 2)_BS-MS_R</i>	AATACCCACTTTCTACAATACTTATACAC
<i>Dlx2 (region 4)_BS-MS_F</i>	TTTTAAGTATGTGATTAAGGTTTTGGG
<i>Dlx2 (region 4)_BS-MS_R</i>	CCATCTACTCCAATTTCCAAC TAAC
<i>Gbx2 (region 3)_BS-MS_F</i>	GATTGTTGGATGGAGTTGAGTTTT
<i>Gbx2 (region 3)_BS-MS_R</i>	CAATACCCTCCTTTACTCCTTAACC
<i>Gfap_BS-MS_F</i>	ATTAGTTAGTTTGGTGGGTTTTTTG
<i>Gfap_BS-MS_R</i>	ATCAAAAACAAATTTAATCCAACCC
<i>Gsh2_BS-MS_F</i>	ATAAGGATATTTGAGAATTGATGTAGTTTG
<i>Gsh2_BS-MS_R</i>	ACCATTTAAACTAAAATAACCAATACATTT
<i>Insl6_BS-MS_F</i>	AGGTTATGAAATTATAAAAGGGATTT
<i>Insl6_BS-MS_R</i>	CCCTATACCAACAAAACAACACATA
<i>Nkx2-2_BS-MS_F</i>	ATAGAAAGGAGGGGGTAAAGAATTT
<i>Nkx2-2_BS-MS_R</i>	CCTATTCCTCTCCTAAATTTCCAAC
<i>Sp8_BS-MS_F</i>	TATTGGTATTGGTTTTTTTTGTGGTT
<i>Sp8_BS-MS_R</i>	TCTCAAATAACCCCACTATACCTTTC
<i>Sparcl1_BS-MS_F</i>	AATTTGGAGGTTGGTATTATAGGGT
<i>Sparcl1_BS-MS_R</i>	AAAAACAACAACCTTCATTTTCCAA
<i>Pdgfra_BS-MS_F</i>	GTGTTTTGGGTTTTTTGGTTTGT
<i>Pdgfra_BS-MS_R</i>	CCACTTATCTAATCCTACCTTTATTTTC

References for Supporting Online Material

1. V. Coskun *et al.*, *Proc Natl Acad Sci U S A* **105**, 1026 (Jan 22, 2008).
2. W. Ge *et al.*, *J Neurosci Res* **69**, 848 (Sep 15, 2002).
3. S. J. Cokus *et al.*, *Nature* **452**, 215 (Mar 13, 2008).
4. M. Kurita, T. Kuwajima, I. Nishimura, K. Yoshikawa, *J Neurosci* **26**, 12003 (Nov 15, 2006).
5. T. Chen, Y. Ueda, S. Xie, E. Li, *J Biol Chem* **277**, 38746 (Oct 11, 2002).
6. F. He *et al.*, *Nat Neurosci* **8**, 616 (May, 2005).
7. T. H. Kim *et al.*, *Nature* **436**, 876 (Aug 11, 2005).
8. T. S. Mikkelsen *et al.*, *Nature* **448**, 553 (Aug 2, 2007).
9. M. Weber *et al.*, *Nat Genet* **37**, 853 (Aug, 2005).
10. A. Smallwood, P. O. Esteve, S. Pradhan, M. Carey, *Genes Dev* **21**, 1169 (May 15, 2007).
11. R. Cao, Y. Zhang, *Mol Cell* **15**, 57 (Jul 2, 2004).
12. J. D. Cahoy *et al.*, *J Neurosci* **28**, 264 (Jan 2, 2008).
13. G. L. Sen, J. A. Reuter, D. E. Webster, L. Zhu, P. A. Khavari, *Nature* **463**, 563 (Jan 28).
14. A. M. Broske *et al.*, *Nat Genet* **41**, 1207 (Nov, 2009).
15. R. Straussman *et al.*, *Nat Struct Mol Biol* **16**, 564 (May, 2009).
16. R. Lister *et al.*, *Nature* **462**, 315 (Nov 19, 2009).
17. T. A. Rauch, X. Wu, X. Zhong, A. D. Riggs, G. P. Pfeifer, *Proc Natl Acad Sci U S A* **106**, 671 (Jan 20, 2009).
18. M. M. Suzuki, A. Bird, *Nat Rev Genet* **9**, 465 (Jun, 2008).